JGR Solid Earth

RESEARCH ARTICLE
10.1029/2023JB026735

Continental Residual Topography Extracted From Global Analysis of Crustal Structure

Simon N. Stephenson[1], **Mark J. Hoggard**[2], **Megan C. Holdt**[3], **and Nicky White**[3]

[1]Department of Earth Sciences, University of Oxford, Oxford, UK, [2]Research School of Earth Sciences, Australian National University, Canberra, ACT, Australia, [3]Bullard Laboratories, Department of Earth Sciences, University of Cambridge, Cambridge, UK

Key Points:

- Continental residual topography estimated using 26,725 crustal thickness and 4,067 seismic velocity constraints
- Crustal velocity to density conversion scheme developed to correct for crustal density variations
- Residual topography varies from ~1 to 2 km over ~1,000 km wavelengths, consistent with a range of geological observations

Supporting Information:

Supporting Information may be found in the online version of this article.

Correspondence to:

S. N. Stephenson,
simon.stephenson@earth.ox.ac.uk

Citation:

Stephenson, S. N., Hoggard, M. J., Holdt, M. C., & White, N. (2024). Continental residual topography extracted from global analysis of crustal structure. *Journal of Geophysical Research: Solid Earth*, *129*, e2023JB026735. https://doi.org/10.1029/2023JB026735

Received 15 MAR 2023
Accepted 29 MAR 2024

Author Contributions:

Conceptualization: Simon N. Stephenson, Nicky White
Data curation: Simon N. Stephenson, Megan C. Holdt
Formal analysis: Simon N. Stephenson, Mark J. Hoggard
Funding acquisition: Simon N. Stephenson, Nicky White
Investigation: Simon N. Stephenson, Mark J. Hoggard, Megan C. Holdt
Methodology: Simon N. Stephenson, Mark J. Hoggard, Megan C. Holdt, Nicky White
Project administration: Simon N. Stephenson, Nicky White
Resources: Simon N. Stephenson, Mark J. Hoggard, Megan C. Holdt
Software: Simon N. Stephenson

Abstract Continental topography is dominantly controlled by a combination of crustal thickness and density variations. Nevertheless, it is clear that some additional topographic component is supported by the buoyancy structure of the underlying lithospheric and convecting mantle. Isolating these secondary sources is not straightforward, but provides valuable information about mantle dynamics. Here, we estimate and correct for the component of topographic elevation that is crustally supported to obtain residual topographic anomalies for the major continents, excluding Antarctica. Crustal thickness variations are identified by assembling a global inventory of 26,725 continental crustal thickness estimates from local seismological data sets (e.g., wide-angle/refraction surveys, calibrated reflection profiles, receiver functions). In order to convert crustal seismic velocity into density, we develop a parametrization that is based upon a database of 1,136 laboratory measurements of seismic velocity as a function of density and pressure. In this way, 4,120 new measurements of continental residual topography are obtained. Observed residual topography mostly varies between ±1 and 2 km on wavelengths of 1,000–5,000 km. Our results are generally consistent with the pattern of residual depth anomalies observed throughout the oceanic realm, with long-wavelength free-air gravity anomalies, and with the distribution of upper mantle seismic velocity anomalies. They are also corroborated by spot measurements of emergent marine strata and by the global distribution of intraplate magmatism that is younger than 10 Ma. We infer that a significant component of residual topography is generated and maintained by a combination of lithospheric thickness variation and sub-plate mantle convection. Lithospheric composition could play an important secondary role, especially within cratonic regions.

Plain Language Summary Plate tectonic theory holds that the horizontal movement of tectonic plates drives crustal thickening and the formation of mountain ranges where plates collide, and crustal thinning in rift basins where plates diverge. The dominance of this process, however, obscures a key secondary source of topographic variation caused by density variations within the underlying mantle. In this study, we compile two new databases. The first is a global compilation of crustal thickness and seismic velocity measurements obtained from seismic experiments. The second is a compilation of laboratory analyses of seismic velocity in crustal rocks as a function of temperature, pressure and density. We combine these data sets to accurately map that component of continental topography caused by crustal thickness and density variations and use it to isolate the secondary, residual component supported by the mantle. We find that a substantial proportion of topography is supported by the temperature and chemical structure of the mantle and is manifest as topographic swells and basins that can occur within interiors of tectonic plates, have amplitudes of up to 2 km, and length scales ranging from hundreds to thousands of kilometers. Independent geologic evidence suggests that some of these topographic features developed over million-year time scales.

1. Introduction

It has long been recognized that continental topography is dominated by the isostatic effects of crustal thickness and density variations (Airy, 1855; Pratt, 1855). Nonetheless, it is clear that the density structure of both the lithospheric and sub-lithospheric mantle also contribute to the elevation of Earth's surface (e.g., Hager et al., 1985; Jordan, 1978; Lamb et al., 2020; D. McKenzie, 1978; Menard, 1965; Pekeris, 1935). Thick, dense lithospheric roots and convective downwellings generate topographic lows, while thin lithospheric mantle and convective upwelling support topographic highs (Bird, 1979; Hager & Richards, 1989; Hager et al., 1985). The surface expression of some—or sometimes all—of these processes is referred to as dynamic topography. Dynamic topography can be defined in several different ways and its meaning can be a matter of controversy and confusion

Supervision: Simon N. Stephenson, Nicky White
Validation: Simon N. Stephenson, Nicky White
Visualization: Simon N. Stephenson, Mark J. Hoggard, Megan C. Holdt, Nicky White
Writing – original draft: Simon N. Stephenson
Writing – review & editing: Simon N. Stephenson, Mark J. Hoggard, Megan C. Holdt, Nicky White

(Colli et al., 2016; Forte & Rowley, 2022; Hoggard et al., 2021; Molnar et al., 2015). The most restrictive definition includes only vertical tractions imparted on the base of the plate by active flow within the mantle, discounting any isostatic topography associated with the buoyancy anomalies that drive this flow (Molnar et al., 2015). A more widely held view is that all topography arising from sub-plate mantle density structure should be included (e.g., T. W. Becker et al., 2014; Conrad & Husson, 2009; Crosby & McKenzie, 2009; Faccenna & Becker, 2020; Hager et al., 1985; D. P. McKenzie et al., 1974; Ricard et al., 1993; Steinberger et al., 2019). Finally, a broader definition holds that dynamic topography is any topography supported by sub-crustal processes, including buoyancy variations that reside within the lithospheric mantle (Forte & Rowley, 2022; Forte et al., 1993; Glišović & Forte, 2016; Moucha et al., 2008). Regardless of its exact definition, the presence, amplitude and spatial characteristics of dynamic topography contain pertinent information about geodynamic processes that operate within Earth's interior (e.g., Arnould et al., 2018; Austermann et al., 2017; Ghelichkhan et al., 2021; Hager et al., 1985; Hoggard et al., 2016; Hoggard, Parnell-Turner, & White, 2020; Holdt et al., 2022; Lithgow-Bertelloni & Silver, 1998; Richards et al., 2023; Spasojevic & Gurnis, 2012; Steinberger et al., 2019). Attempts to place constraints on the present-day pattern of dynamic topography have therefore garnered substantial attention by the geodynamical community (D. R. Davies et al., 2023; Flament et al., 2013; Hoggard et al., 2021).

In the oceanic realm, both the thickness and average density of the crust and its sedimentary cover are accurately measured in many locations, which makes correcting for crustal isostatic effects straightforward provided that the depth to seabed, basement and Moho can be accurately estimated (Hoggard et al., 2017; Holdt et al., 2022; Winterbourne et al., 2009). Furthermore, oceanic lithosphere cools and thickens as a function of time, meaning that depth to basement, after correcting for crustal and sedimentary loading, follows a predictable age-depth relationship (Afonso et al., 2007; Parsons & Sclater, 1977; Richards et al., 2018; Stein & Stein, 1992). Comparison of observed basement depths to this prediction yields estimates of residual bathymetry, which is commonly interpreted as a proxy for dynamic support by sub-plate mantle convection (e.g., Cazenave et al., 1988; Cochran & Talwani, 1977; Hoggard et al., 2016; Menard, 1965). The past two decades, in particular, have seen the acquisition and compilation of high-quality seismic reflection and wide-angle/refraction profiles, enabling accurate corrections for crustal and sedimentary loading to be obtained which yields detailed maps of oceanic residual bathymetry of unparalleled fidelity (Hoggard et al., 2017; Holdt et al., 2022; Winterbourne et al., 2009, 2014).

These advances in constraining oceanic residual topography have highlighted several important discrepancies between observational inferences and numerical predictions of dynamic topography. Particular controversies surround the proposed amplitude of dynamic topography at long wavelengths (i.e. ∼10,000 km; spherical harmonic degree $l = 2$), and the relative contributions of lithospheric, asthenospheric, and deep mantle buoyancy anomalies to the observed residual topographic field (see e.g. D. R. Davies et al., 2019, 2023; Forte & Rowley, 2022; Hoggard et al., 2016, 2017, 2021; Holdt et al., 2022; Molnar et al., 2015; Richards et al., 2020, 2023; Steinberger et al., 2019; Wang et al., 2022; Watkins & Conrad, 2018; Yang & Gurnis, 2016). Our ability to shed light on these controversies is hampered, in part, by a paucity of reliable observational constraints for residual topography throughout the continental realm.

Continental residual topography is poorly constrained due to a combination of factors. For example, the generally more protracted geologic history of the continents, including orogenic cycles, erosion, and reworking of crustal rocks, and the extraction, intrusion and fractionation of melts, results in a substantially larger variability in crustal thickness and density structure in comparison to oceanic settings (Christensen & Mooney, 1995; Lamb et al., 2020; Laske et al., 2013; Szwillus et al., 2019). Crustal density structure is generally poorly constrained, resulting in propagation of substantial uncertainty into corrections for crustal isostasy (Guerri et al., 2015; Lamb et al., 2020; Molnar et al., 2015). For example, a representative change of ±0.1 Mg m^{-3} in continental crustal density can result in more than ±1.0 km of air-loaded topography, which is comparable to expectations for the total amplitude of dynamic topography (Hoggard et al., 2021). Furthermore, attempts to constrain continental residual topography to date have tended to rely on global grids of crustal thickness and density (e.g., Forte & Rowley, 2022; Lamb et al., 2020; Pari & Peltier, 2000; Steinberger, 2016; Wang et al., 2022). These grids not only contain large uncertainties, but they are also often extrapolated into regions of sparse data coverage and are therefore liable to contain gridding artifacts (Szwillus et al., 2019). A simple way to side-step this issue is to exploit continental free-air gravity anomalies as a proxy for sub-plate topographic support (Hoggard et al., 2016; D. McKenzie & Fairhead, 1997; Molnar et al., 2015). Unfortunately, the relationship between dynamically

supported topography and free-air gravity anomalies might not be quite as simple as the linear transfer function used in these studies, since it depends on both the depth and length scale of the driving mantle density anomaly (Colli et al., 2016; Parsons & Daly, 1983). Analogous to developments in the oceanic realm, an alternative approach in continental settings takes advantage of the proliferation of high-resolution active and passive source seismic experiments to generate relatively accurate local estimates of residual topography (e.g., Davis et al., 2012; Levandowski et al., 2014). This approach circumvents the use of gravity anomalies and/or interpolated crustal grids. The increase in number of passive seismic experiments over the last decade also provides more comprehensive geographical coverage of crustal thickness and velocity structure than was previously available when these crustal models were built (Laske et al., 2013). Nonetheless, accurately constraining local density structure in order to remove the effects of crustal isostasy, and to quantify its uncertainty, remains a significant challenge in the analysis of continental residual topography (Barton, 1986; Brocher, 2005; Christensen & Mooney, 1995; Hoggard et al., 2021; Lachenbruch & Morgan, 1990; Lamb et al., 2020; Levandowski et al., 2014; Ludwig et al., 1970; Molnar et al., 2015).

Our goal in this study is to extensively map global residual topography in the continental realm using local measurements of crustal thickness and density structure, while estimating and reducing its uncertainty. We use the term "residual topography" to represent all topography that is not supported by crustal thickness and/or density variations. We thereby specifically avoid the need to discriminate between residual topography that is supported by static sub-crustal density anomalies and that which is supported by mantle flow (compare the dynamic topography definitions of Forte et al. (1993) and Molnar et al. (2015)). Our global study is divided into three parts. First, we compile a global database of crustal thickness and seismic velocity measurements from a broad range of published seismological experiments. Second, we assemble a separate database of published laboratory analyses on seismic velocity in rocks as a function of pressure, which we then use to calibrate a crustal seismic velocity-to-density conversion scheme as a function of pressure and temperature. Finally, we calculate residual topography and uncertainties at each location within our database and explore their relationship to a range of independent geologic observations.

2. Continental Crustal Database

Our aim is to construct a comprehensive database of crustal thickness and density estimates in order to calculate residual topographic anomalies in the continental realm (Figure 1). Due to significant trade-offs between thickness and density of crustal layers obtained by gravity modeling, we restrict ourselves to crustal constraints determined solely by seismic imaging. Our database, SeisCruST, contains 26,725 seismically-determined estimates of crustal thickness, which includes 3,716 constraints calculated from refraction/wide-angle experiments, 136 from deep seismic reflection profiles, 22,811 from analysis of receiver functions, and 62 from other sources (Database 1a in Supporting Information S1; Stephenson, Hoggard, Holdt, & Galbraith-Olive, 2024). For completeness, we list a further 7,146 observations from the global Earthscope Automated Receiver Survey, but do not otherwise use them in our analysis since these data are generated by an automatic algorithm that we have found to produce particularly noisy results. We have also avoided incorporating tomographic imaging studies since they are subject to varying degrees of regularization and result in variations in crustal structure being smoothed over wide geographic regions. For the avoidance of confusion, throughout this text and within our database, the term "crustal thickness" should be taken to mean depth from the surface to the Moho discontinuity inclusive of any sedimentary cover.

2.1. Data Categorization and Distribution

Our database is composed of two main suites of data, based upon active and passive source seismological approaches, respectively. We exploit the Global Seismic Catalog of the United States Geological Survey (i.e., USGS GSC) database, an extensive catalog of crustal thickness estimates determined using a range of techniques that was initially compiled by Christensen and Mooney (1995), updated by Mooney (2015) and Mooney et al. (2023). Continuous, interpolated crustal thickness models based upon iterations of this database have been published by Mooney et al. (1998) (i.e., CRUST5.1), Bassin (2000) (i.e., CRUST2.0), Laske et al. (2013) (i.e., CRUST1.0), Szwillus et al. (2019) and Mooney et al. (2023) (i.e., ECM1). This database is filtered for crustal thickness estimates determined by seismic reflection and refraction using controlled sources (e.g., Figures 2a and 2b) that were acquired over a period from 1950 to 2020. Modeling and interpretation of data collected by these experiments has substantially improved over the last 40 years. Prior to ~1980, for example, wide-angle

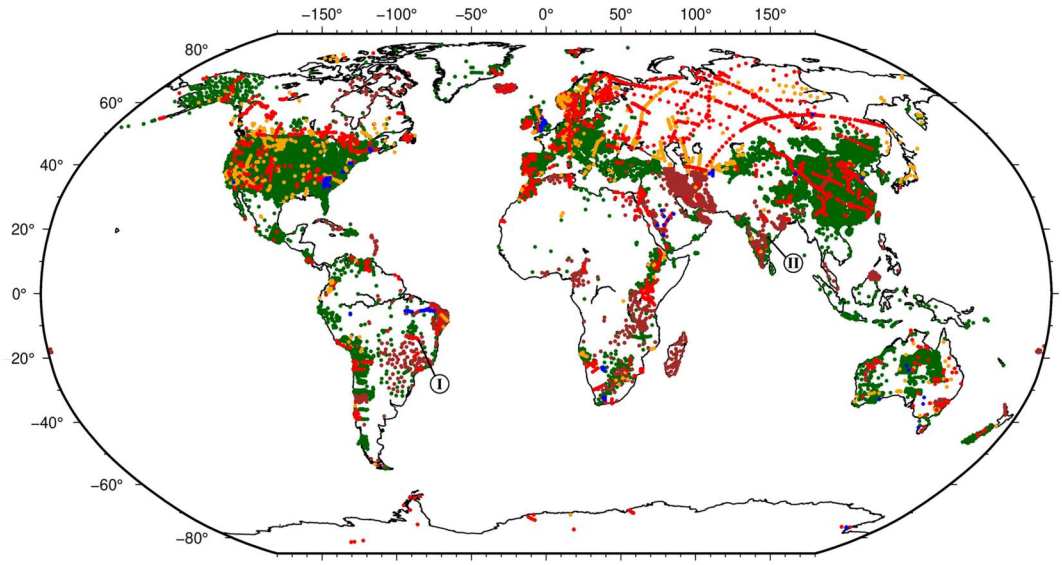

Figure 1. Locations and categories of crustal thickness measurements. Whole, unfiltered database including Antarctica, Greenland and regions of lithospheric flexure on Robinson projection. Green = P-to-S and S-to-P receiver functions (including H-κ stacking, common conversion point stacking, receiver function forward and inverse modeling); brown = surface wave and receiver function joint inversions; yellow = wide-angle surveys published prior to 1980; red = wide-angle surveys published post-1980; blue = deep reflection profiles. I and II = location of seismic experiments shown in Figure 2.

experiments usually relied upon the slope-intercept approach to constrain the number, depth and thickness of crustal layers, each of which would be assumed to have a constant velocity. This approach tends to underestimate crustal thickness since it is unable to capture vertical velocity gradients within layers and their associated diving rays (White et al., 1992). Post-1980 experiments generally rely upon numerical modeling that can account for this

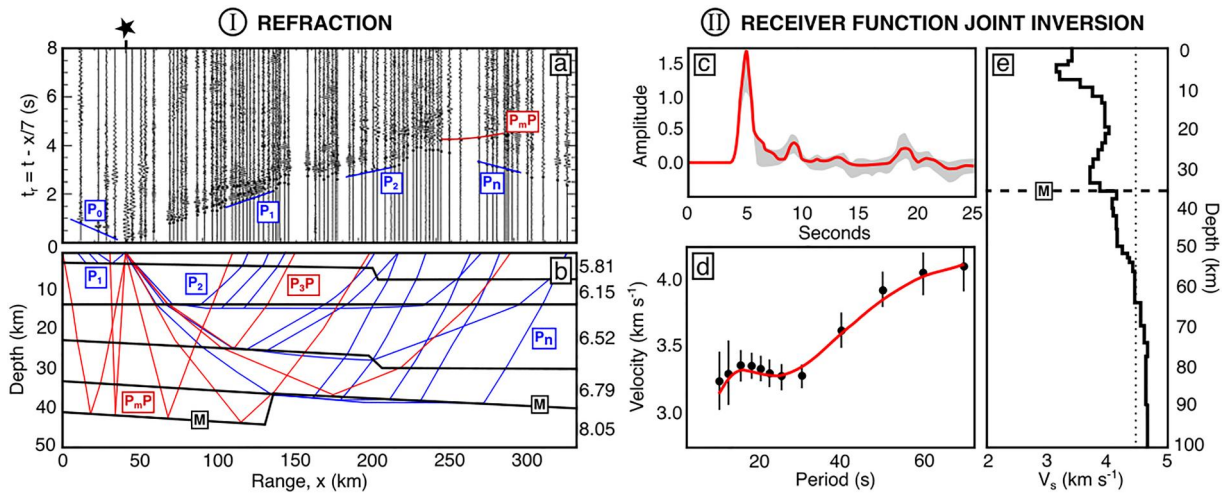

Figure 2. Controlled source and passive seismic experiments yielding both crustal thickness and seismic velocity estimates. *Left-hand panel*, (I) = refraction experiment from Porangatu wide-angle survey, Tocantis Province, central Brazil (Soares et al., 2006). (a) P-wave record section for shot 1. Star = shot location. Black lines = seismic records at receivers located along transect. Blue lines = interpreted arrivals of refracted rays; P_0 = direct arrival; P_1 and P_2 = internal crustal refracted arrivals; P_n = Moho refracted arrival. Red lines = interpreted arrivals of reflected rays; P_mP = Moho reflected arrival. (b) Simplified redrawing of raypath model (after Soares et al., 2006). Black lines = interpreted internal boundaries calculated by inverse modeling; blue lines = refracted ray paths; red lines = reflected ray paths; M = Moho; P_1, P_2, P_n = rays refracted at first, second and Moho layers, respectively; P_3P, P_mP = ray reflected from third crustal layer and Moho, respectively. Internal layer P-wave velocities indicated at right-hand side of panel. For detailed transect location, see Figure 1 and Soares et al. (2006). *Right-hand panel*, (II) = joint receiver function and surface wave inverse model for station HYB, Dharwar Craton, central India (Gilligan & Priestley, 2018). (c) Gray band = 1σ bounds on observed receiver function; red line = optimal fitted receiver function obtained from inverse modeling. (d) Black circles with error bars = observed Rayleigh wave group velocity as a function of period; red curve = optimal dispersion curve from inverse modeling. (e) Dotted black line = initial velocity model prior to inverse modeling; solid black line = final velocity model; dashed black line labeled M = Moho.

effect and are therefore not subject to this systematic bias. Techniques for migration of reflection data have also improved over this period, which permits more precise estimation of the subsurface velocity structure. We have supplemented the database of controlled-source crustal thickness constraints from the USGS GSC database with a small number of additional refraction data.

Since the 2000s, there has been a proliferation in the number of passive-source seismic experiments used to estimate crustal thickness using teleseismic *P* arrivals, their *S*-wave conversions and Moho reverberations. Here, we compile a new global database of crustal thickness estimates determined by these receiver functions. We supplement this new compilation with receiver function constraints assembled by Mooney et al. (2023). By far the most commonly used technique is the H-κ stacking method described by L. Zhu and Kanamori (2000), which involves searching for the combination of Moho depth, H, and bulk ratio of crustal velocities (i.e., $\overline{V}_P/\overline{V}_S = \kappa$), that maximizes the amplitude sum of *P*-to-*S* conversions beneath a given seismic receiver. A second approach designed to reduce trade-offs between H and κ combines receiver functions, which provide information about sharp discontinuities such as the Moho, with surface wave dispersion curves, which are sensitive to absolute shear-wave velocity as a function of depth (e.g., Figures 2c–2e). Joint inversion of these two passive seismic data sets yields an absolute *S*-wave velocity profile beneath the receiver from which the Moho can be interpreted (e.g., Gilligan & Priestley, 2018; Julià et al., 2009). Finally, inverse modeling of receiver functions alone can also be used to provide velocity constraints although results are less reliable than those obtained through joint inverse modeling. A complete table of our data sources, crustal thickness estimates and processing procedures is provided in Supporting Information S1 and the documentation to the SeisCruST database (Stephenson, Hoggard, Holdt, & Galbraith-Olive, 2024).

Spatial coverage of crustal thickness estimates is uneven (Figure 1). The most densely-imaged regions are western and northern Europe, eastern China and the United States. Western Europe has been extensively imaged by wide-angle refraction studies, whose acquisition dates span the second half of the twentieth century. The EarthScope program in the US has yielded crustal thickness estimates at approximately 70 km spacing across both the contiguous US and Alaska (e.g., Ma & Lowry, 2017). Similarly, the IberArray in Iberia has resulted in a dense coverage of crustal thickness estimates calculated using the H-κ technique. Crustal thickness estimates in China exploit both the *Chinese National Seismic Network* and also a dense pattern of local deployments that have been generally analyzed using the H-κ stacking technique. The AusArray program is steadily increasing the density of measurements in remote northern, central and western Australia (Gorbatov et al., 2020; Kennett et al., 2023). While sometimes densely imaged at local scales, large portions of central and northern Africa, southeast Asia, northeastern Siberia, Canada, the Amazon, Argentina, and the Middle East are only sparsely imaged. The majority of the data from Siberia come from the results of peaceful nuclear explosions, which were carried out between the 1950s and 1980s, but were largely published in the 1990s (see, e.g., Benz et al., 1992). Note that, with the exception of the onshore portion of the Icelandic Plateau, we have not included data from continental shelves or the oceanic realm.

2.2. Global Crustal Thickness and Velocity Structure

Our database of crustal thickness estimates, SeisCruST, is shown in Figure 3a. Two regions of significantly thicker crust occur in the Tibetan and Andean Plateaux, where crust can locally exceed 80 km in thickness. In cratonic regions such as Siberia; northern and western Fennoscandia; southern and central Africa; central South America; and eastern, northern and central North America, crust is generally between 40 and 60 km thick. In western Europe, north Africa, western North America, Alaska, southern South America, and eastern Asia, crust is generally less than ~40 km and locally <30 km thick. Global mean crustal thickness in our database is 39.7 ± 9.6 km (one standard deviation), which encompasses all 26,725 measurements across all tectonic settings averaged within ~10,735 bins of $0.5° \times 0.5°$. Note that we have not weighted measurements for tectonic setting in calculating this value (cf. Christensen & Mooney, 1995; Mooney et al., 2023).

Seismic velocity profiles are available at 4,113 of the sites in our crustal database (N.B. this total includes 44 profiles located in Greenland and Antarctica that we later exclude from our analysis; Database 1b in Supporting Information S1). Where refraction experiments were carried out, *P*-wave velocity profiles, $V_P(z)$, are generally available. Bulk crustal V_P estimates, $\overline{V}_P$, are shown at these locations in Figure 3b. Values of $\overline{V}_P$ are markedly higher in Archean shields such as Canada, Fennoscandia, and Siberia in comparison to Phanerozoic crust, such as in the western United States and southern Europe. At a subset of locations, shear-wave velocity profiles, $V_S(z)$,

10.1029/2023JB026735

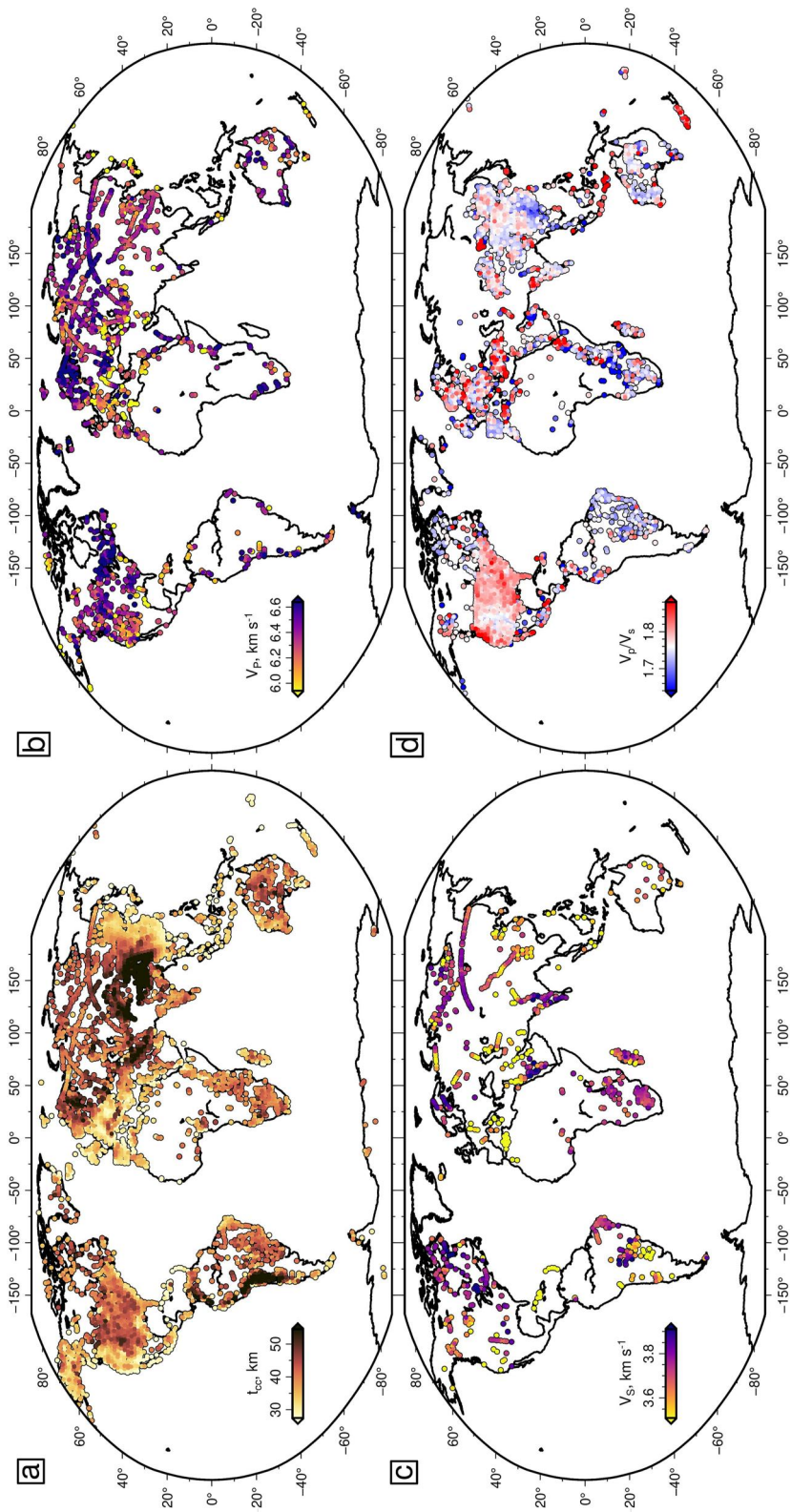

Figure 3. Global seismic crustal structure (SeisCruST) determined by wide-angle, deep reflection and receiver function analysis (Stephenson, Hoggard, Holdt, & Galbraith-Olive, 2024). (a) 26,725 spot estimates of crustal thickness, t_{cc} estimated by controlled-source wide-angle and reflection experiments and passive source receiver function analysis. (b) Bulk crustal *P*-wave velocity $\overline{V}_P$ estimated predominantly by wide-angle experiments and receiver function inverse modeling. (c) Bulk crustal S-wave velocity $\overline{V}_S$ estimated predominantly by wide-angle, receiver function inverse modeling and joint surface wave–receiver function inverse modeling. (d) Bulk crustal $\overline{V}_P/\overline{V}_S$ estimated by *H*-κ stacking of receiver functions.

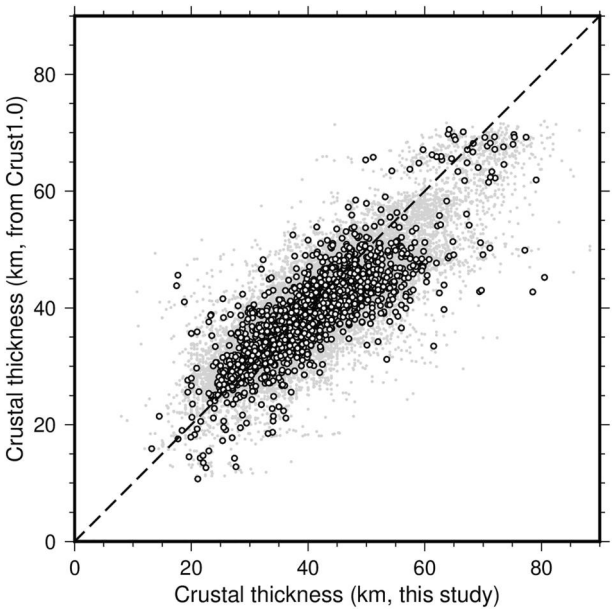

Figure 4. Local estimates of crustal thickness versus values at same location from global Crust1.0 model (Laske et al., 2013). Small gray circles = all data; large white circles = mean values within 1° × 1° geographic bins; Pearson's correlation coefficient, $r = 0.82$.

have been estimated from either refraction experiments, receiver function inversions, or receiver function and surface wave joint inversions (Figure 3c). Bulk shear velocities, $\overline{V}_S$, are noisier than $\overline{V}_P$ estimates and have significantly more limited geographic coverage. Nonetheless, values of $\overline{V}_S$ are greater beneath the Canadian, Brazilian and Indian Shields than beneath eastern Australia, Madagascar, eastern China and southern Brazil. Finally, at 17,003 locations, application of the H-κ stacking approach has yielded estimates of bulk $\overline{V}_P/\overline{V}_S$ (Figure 3d). Any putative relationship between first-order geological setting and $\overline{V}_P/\overline{V}_S$ ratio is less apparent and the data are significantly more noisy. For example, western Europe, Anatolia, Southeast Asia and the East African Rift are characterized by highly variable $\overline{V}_P/\overline{V}_S$ values. The highest values are found in Java and Sumatra, New Zealand, the Cascades, Anatolia, and Afar. Despite the more significant scatter, in North America there is a clear transition from higher values of $\overline{V}_P/\overline{V}_S$ in the east and west to lower values on the Colorado Plateau. Eastern South America, Iberia, southern Africa, western Australia and southeastern China are also generally characterized by lower $\overline{V}_P/\overline{V}_S$ values.

It is instructive to compare our spot measurements of crustal thickness to interpolated global grids that are widely used within the geophysical community. Figure 4 shows the relationship between our database and that of Crust1.0 at the same sites (Laske et al., 2013). There is a strong correlation between the two data sets (i.e., Pearson's correlation coefficient, $r = 0.82$), which suggests that the general trends in the local data are well represented in Crust1.0. However, Crust1.0 systematically under-predicts the thickness of the thickest crust by 5–10 km. Furthermore, there is significant, ±~15 km scatter between local observations and the smoothed Crust1.0 model. This scatter persists when our crustal thickness estimates are spatially averaged into 1° × 1° bins.

3. Correcting for Crustal Isostasy

We are primarily interested in determining the component of topographic elevation that is generated by sub-crustal buoyancy structure. Our global database of point-wise crustal thickness and seismic velocity constraints can be used to determine the component of topography supported by crustal thickness and density variations. We must correct observed topographic measurements for this crustal isostasy in order to estimate the residual component resulting from mantle buoyancy structure. Residual topography, e_r, is defined as

$$e_r = e + C_c \tag{1}$$

where e is the observed surface elevation, taken from the ETOPO1 global topographic model of J. J. Becker et al. (2009) and C_c is the correction for local crustal isostasy. Note that both mathematical symbols for parameters and the values of constants used in this study are summarized in Table 1. We low-pass filter observed topography for wavelengths >30 km to reflect the horizontal resolution of crustal thickness estimates and to remove the shortest-wavelength topographic features that could be flexurally supported.

3.1. Simple Crustal Thickness Correction

Under the assumption of isostatic equilibrium and constant crustal density, ρ_{cr}, the correction for crustal isostasy, C_c, reduces to a simpler crustal thickness correction, C_t, given by

$$C_t = (t_{cr} - t_{cc})\left(\frac{\rho_a - \rho_{cr}}{\rho_a}\right), \tag{2}$$

Table 1
Definition and Values for Parameters Used in This Study

	Parameter	Symbol	Value	Units
Continental Crust	Reference crustal density	ρ_{cr}	2.84	Mg m^{-3}
	Local crustal density	ρ_{cc}		Mg m^{-3}
	Density at surface temperature and pressure (s.t.p.)	$\rho_{\circ}$		Mg m^{-3}
	Reference crustal thickness	t_{cr}	32.1	km
	Local crustal thickness	t_{cc}		km
	Thermal expansivity at reference T	α_0	$(1.0 \pm 0.5) \times 10^{-5}$	K^{-1}
	Thermal expansivity constant T derivative	α_1	$(2.9 \pm 0.5) \times 10^{-8}$	K^{-2}
	Bulk modulus	K_{cc}	90 ± 20	GPa
	P-wave velocity	V_P		km s^{-1}
	S-wave velocity	V_S		km s^{-1}
Mantle	Mantle density at s.t.p.	$\rho_{m_{\circ}}$	3.33	Mg m^{-3}
	Asthenospheric density	ρ_a	3.25 ± 0.01	Mg m^{-3}
	Reference mantle density	ρ_{mr}		Mg m^{-3}
	Density reduction due to depletion	$\Delta\rho$		Mg m^{-3}
	Depleted mantle density	ρ_m^*		Mg m^{-3}
	Depth to lithosphere-asthenosphere boundary	z_l		km
	Bulk modulus	K_m	140	GPa
	Specific heat capacity	C_p	1,187	J kg^{-1} K^{-1}
	Thermal expansivity at reference T	α_0	2.832×10^{-5}	K^{-1}
	Thermal expansivity constant T derivative	α_1	0.758×10^{-8}	K^{-2}
	Potential temperature	T_p	1,333	°C
	Asthenospheric temperature	T_a		°C
Residual topography	Residual topography	e_r		km
	Density correction	C_ρ		km
	Thickness correction	C_t		km
	Binned residual topography	$\overline{e}_r$		km
	Standard error on binned residual topography	$\sigma_{\overline{e}_r}$		km
	Binning weights	w		
General	Density	ρ		Mg m^{-3}
	Temperature	T		°C
	Pressure	P		MPa
	Depth	z		km
	Elevation	e		km
	Surface temperature	T_0	10	°C
	Acceleration due to gravity	g	9.81	m s^{-2}
	Seismic velocity	v		km s^{-1}
	Temperature-corrected seismic velocity	v_c		km s^{-1}
Heat flow	Surface heat flux	q_0	59 ± 14	mW m^{-2}
	Moho heat flux	q_m	30 ± 10	mW m^{-2}
	Thermal conductivity	k	2.5	W m^{-1} K^{-1}
	Radiogenic heat production decay lengthscale	h_r	10 ± 5	km

where t_{cc} is the local crustal thickness, t_{cr} is the thickness of a reference column of continental crust at sea level, and ρ_a is the density of asthenospheric mantle. This correction essentially adjusts locally observed topography for variations in crustal thickness. Provided that crustal thickness is not correlated with e_r, then the value of the parameters in Equation 2 can be estimated from a plot of observed elevation versus observed crustal thickness.

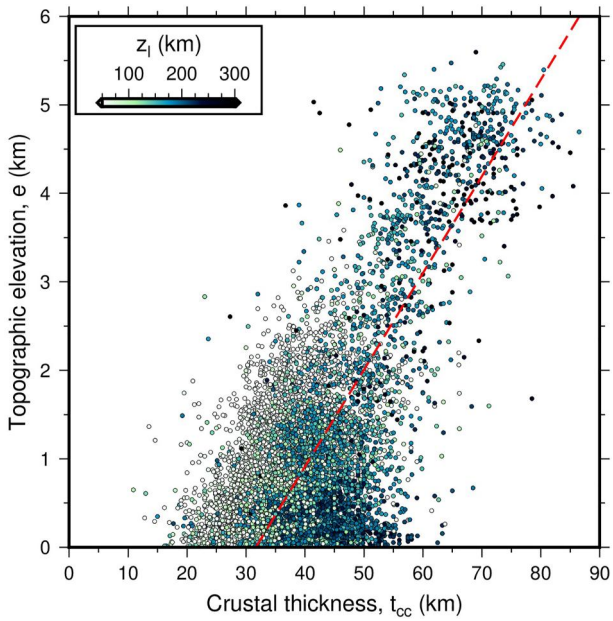

Figure 5. Relationship between estimates of crustal thickness in 0.5 × 0.5° bins and topographic elevation. Circles = mean crustal thickness within geographic bin colored by lithospheric thickness, z_l, from Hoggard, Czarnota, et al. (2020), which is based upon the surface wave tomographic model of Schaeffer and Lebedev (2013); red dashed line = optimal fit of unbiased linear regression of Marks and Sandwell (1991), Pearson's correlation coefficient, $r = 0.67$.

There is a demonstrable relationship between the value of t_{cc} in our database and elevation, with a Pearson's correlation coefficient of $r = 0.67$ (Figure 5). The thickest crust (~80 km) beneath the Himalayas and the Andes has a low-pass filtered elevation of up to ~6 km, while the thinnest crust of <25 km thickness is generally located near or below sea level. 30–80 km variations in crustal thickness account for ~5 km of variation in topographic elevation. Hence, it is clear that the primary control on surface elevation is thickness of the continental crust. Accurate accounting for the effects of crustal thickness variation is therefore vital for isolating secondary sources of surface topography, such as crustal density variation and mantle buoyancy structure.

In order to carry out the crustal thickness correction, it is necessary to estimate the value of the ratio $\rho_a(\rho_a - \rho_{cr})^{-1}$ (i.e., the inverse of the constant of proportionality in Equation 2), which is given by the inverse of the slope of the e-t_{cc} relationship. An estimation of its globally averaged value can be obtained directly from Figure 5. Applying the non-biased linear regression method of Marks and Sandwell (1991), which assumes both elevation and crustal thickness data contain uncertainties, yields a value for this ratio of ~9.1 ± 3.9 (i.e., red dashed line on Figure 5). This value is within error of the result of 7.8 obtained by Lamb et al. (2020), who performed a similar analysis using the Crust1.0 global crustal thickness model.

Propagating our estimate of uncertainty in this ratio through Equation 2 demonstrates that a 10 km change in crustal thickness can increase surface elevation from anywhere between 0.8 and 2.0 km, which is too wide a range to be of use in correcting for crustal isostasy. The validity of using a single, global value of $\rho_a(\rho_a - \rho_{cr})^{-1}$ is further undermined by the wide range of geographic locations that lie between sea level and 1 km in elevation, yet are underlain by crust that varies in thickness from less than 20 km to greater than 50 km. This variation can, in part, be explained by the isostatic consequences of variations in the thickness of the lithospheric mantle (Lachenbruch & Morgan, 1990; Lamb et al., 2020). Indeed, within this topographic range, the thickest crust is also underlain by the thickest lithospheric mantle, which acts as a cold, dense root and mitigates the buoyancy effects of thicker crust (Figure 5). However, a further component of the scatter is also likely attributable to variations in crustal density.

We can use a simple calculation to estimate the range of possible crustal density values given that $\rho_a(\rho_a - \rho_{cr})^{-1} = 9.1 \pm 3.9$, provided that we obtain an independent estimate of ρ_a. The density of mantle rocks is generally thought to be dependent on temperature, T, and pressure, P. Thermal expansivity as a function of T at constant P is given by

$$\alpha(T) = -\frac{1}{\rho}\left(\frac{\partial \rho}{\partial T}\right)_P = \alpha_0 + \alpha_1(T + 273) \quad (3)$$

where T is the temperature in degrees Celsius and $\alpha_0 = 2.832 \times 10^{-5}\ \mathrm{K}^{-1}$ and $\alpha_1 = 0.758 \times 10^{-8}\ \mathrm{K}^{-2}$ are constants obtained from laboratory experiments on olivine (Bouhifd et al., 1996), which is the primary constituent of upper mantle rocks. Density as a function of P at constant T depends on the bulk modulus of mantle rocks so that

$$\frac{1}{K_m} = \frac{1}{\rho}\left(\frac{\partial \rho}{\partial P}\right)_T \quad (4)$$

where $K_m = 140$ GPa is the isothermal bulk modulus of the mantle. Integration of Equations 3 and 4 with respect to T and P yields

$$\rho(P,T) \approx \rho_{m_\circ}\left\{\exp\left(\frac{P}{K_m} - \alpha_0(T - T_0) - \frac{\alpha_1}{2}\left[(T+273)^2 - (T_0+273)^2\right]\right)\right\} \quad (5)$$

where $T_0 = 10°C$ is the surface temperature and $\rho_{m_\circ} = 3.33$ Mg m^{-3} is the density of mantle rocks at surface temperature and pressure (D. McKenzie et al., 2005). Assuming it is isentropic, ambient asthenospheric mantle temperature, T_a, can be estimated by integrating

$$\frac{\partial T_a}{\partial z} = \frac{g\alpha(T)z}{C_p} \quad (6)$$

where $g = 9.81$ m s^{-2} is the acceleration due to gravity, $C_p = 1187$ J kg^{-1} K^{-1} is the specific heat capacity of mantle rocks (see Supporting Information S1). We have assumed here that C_p does not vary as a function of P or T, and that α does not vary as a function of P. We estimate pressure at depth z using

$$P(z) = \left(1 \times 10^6\right)\overline{\rho}gz \quad (7)$$

where $\overline{\rho} \sim 3.0$ Mg m^{-3} is the average density of the overburden. If mantle potential temperature, $T_p = 1{,}333°C$, and the thickness of the lithospheric plate is, say, 100–150 km, then Equation 5 yields a mean pressure and temperature-dependent mantle density of $3.24 < \rho_a < 3.27$ Mg m^{-3}. Note that local deviations away from the mean asthenospheric temperature will lead to changes in the value of ρ_a. While these density variations will have an effect upon topographic elevation, we do not consider them a component of the crustal correction since they reside beneath the crust. Variations in ρ_a therefore contribute to residual topography and not to crustal isostasy. Adopting a value of $\rho_a \sim 3.25$ Mg m^{-3} and evaluating the ratio $\rho_a/\left(\rho_a - \overline{\rho}_{cc}\right) \approx 9.1 \pm 3.9$ therefore yields a potential range of $\overline{\rho}_{cc} \sim 2.89 \pm 0.29$ Mg m^{-3} (i.e., uncertainty in bulk crustal density of $\sim\pm10\%$).

Unfortunately, this uncertainty in crustal density is unlikely to be randomly distributed with respect to geographic location. Instead, crustal density varies geographically over distances that are relevant to the ~1,000 km length scale of the mantle component of topography (e.g., compare a Phanerozoic arc terrane, sedimentary basin, and Archean Shield, all of which have systematically different crustal and mantle structures; Christensen & Mooney, 1995; Hoggard et al., 2016). Additionally, due to the combined effects of both pressure and temperature upon density, it is likely that crustal density correlates to some extent with crustal thickness. Taken together, these considerations suggest that while a useful benchmarking exercise, it is unlikely that a linear regression through global crustal thickness and elevation data is the optimal way to estimate this constant of proportionality. Indeed, it cautions against using topographic elevation alone as a proxy for crustal thickness. In order to improve estimates of the correction for crustal isostasy and thereby residual topography, we must better constrain local crustal density by accounting for variations in lithology, pressure and temperature (e.g., Christensen & Mooney, 1995).

3.2. Correction for Local Crustal Density

Under isostatic equilibrium, the topographic correction for local variations in crustal density, C_ρ, is given by

$$C_\rho = t_{cc}\left(\frac{\overline{\rho}_{cc} - \rho_{cr}}{\rho_a}\right), \quad (8)$$

where t_{cc} is the local crustal thickness and $\overline{\rho}_{cc}$ is the local bulk crustal density. In this manner, the complete crustal correction, C_c, from Equation 1 can be recast as $C_c = C_t + C_\rho$ (Figure 6). In order to place tighter bounds on our estimates of local crustal density structure, we turn to local measurements of crustal seismic velocity obtained from seismic experiments.

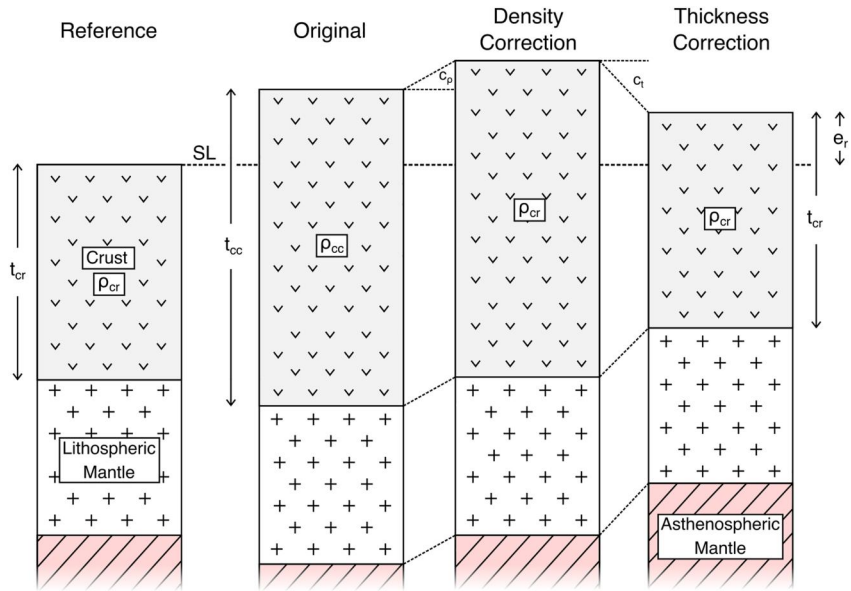

Figure 6. Isostatic balances for crustal density and thickness corrections. Crustal density correction, C_ρ replaces local density of continental crust, $\overline{\rho}_{cc}$, with reference density of continental crust, ρ_{cr}, and is balanced by displacing asthenospheric mantle and air. Crustal thickness correction, C_t replaces local thickness of continental crust, t_{cc}, with reference thickness, t_{cr}. e_r = residual topography after applying corrections. SL = sea level. Note lithospheric mantle is not considered in C_ρ or C_t.

3.2.1. Seismic Velocity-To-Density Conversion

Empirical studies have shown that both V_P and V_S in crustal rocks, measured across a range of pressures, are positively correlated with density at surface temperature and pressure, $\rho_\circ$ (e.g., Christensen, 1974; Christensen & Mooney, 1995; Fountain, 1976; Ji et al., 2009; Stierman et al., 1979; Figure 7). The form of the relationship between seismic velocity and $\rho_\circ$ depends upon the relationship between density and the elastic moduli, which in turn depend upon lithology, pressure and temperature. Constructing a model to fully relate these quantities based on theoretical relationships is challenging, and we instead choose to explore the empirical relationship between velocity and density for typical crustal rocks at crustal depths.

An array of models have been published that relate seismic velocities, usually V_P, to the density of rock samples at standard temperature and pressure (s.t.p.). The most commonly used is the Nafe-Drake relationship, which was published in Ludwig et al. (1970) and formalized as a fourth-order polynomial function by Brocher (2005). Christensen and Mooney (1995) also present an empirical relationship between density and velocity over a range of representative crustal depths and they show that seismic velocities are sensitive to both pressure and temperature. A failure to account for variations in pressure and temperature therefore leads to significant, systematic errors in density estimates, which are pertinent when estimating residual topography. We therefore develop a new pressure- and temperature-dependent scheme, SMV2rho, to estimate crustal density using seismic velocities (Stephenson & Hoggard, 2024).

Seismic velocity, v, as a function of pressure has been empirically shown to be composed of an elastic component, where $\frac{\partial v}{\partial p}$ is linear, and a poro-elastic component, where it decreases exponentially with decreasing pressure. V_P or V_S of a given rock sample as a function of P can therefore be written as

$$\left(\frac{\partial v}{\partial P}\right)_{T,\rho_\circ} = b + ck\exp(-kP) \tag{9}$$

where b is the slope of the linear part of the relationship, c is the amplitude of the velocity drop caused by the opening of pores and microfractures, and k is the decay constant of that velocity drop.

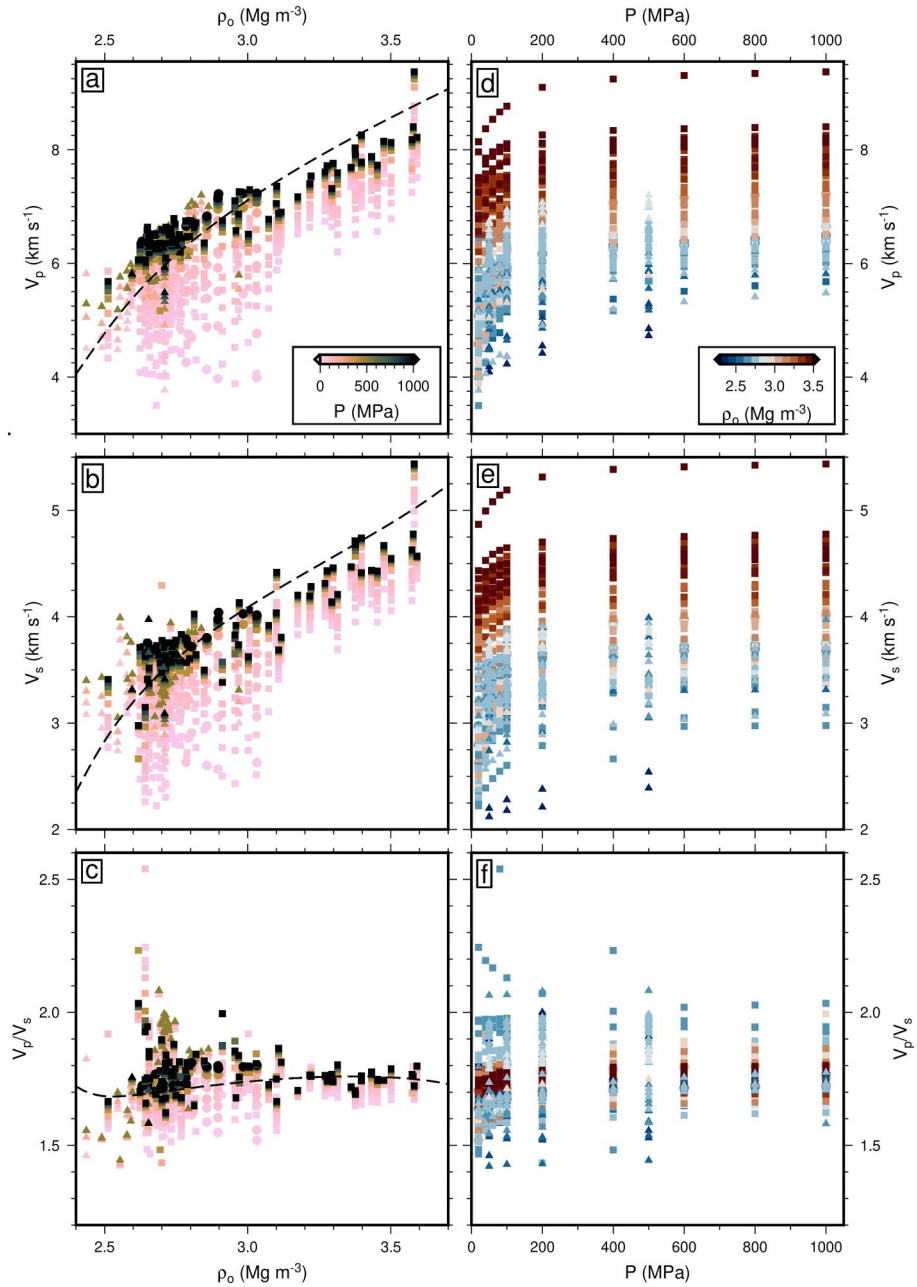

Figure 7. Experimentally determined seismic velocity of crustal rocks as a function of pressure and density at s.t.p. (a) V_P as function of sample density at s.t.p., ρ_o, colored by experimental pressure, P. Circles = igneous rocks; squares = metamorphic rocks; triangles = sedimentary rocks. Black dashed line = pressure- and temperature-independent Nafe-Drake relationship used in previous studies (Brocher, 2005; Ludwig et al., 1970). (b) Same for V_S. Black dashed line = Nafe-Drake relationship extended to V_S using polynomial fit derived by Brocher (2005). (c) Same for V_P/V_S. Black dashed line = Nafe-Drake relationship shown in (a) divided by Brocher's relationship shown in (b) (Brocher, 2005). (d) V_P as a function of P, colored by ρ_o, where white is centered on 2.8 Mg m^{-3}. (e) Same for V_S. (f) Same for V_P/V_S.

We generalize this relationship to account for a range of sample densities at s.t.p. It has been consistently shown that, at a given value of P, seismic velocity varies linearly with ρ_o, such that

$$\left(\frac{\partial v}{\partial \rho_o}\right)_{P,T} = d \tag{10}$$

where d is a constant (e.g., Christensen & Mooney, 1995; Ji et al., 2010). It is possible that $\left(\frac{\partial v}{\partial \rho_\circ}\right)_{P,T}$ may not actually be constant. For example, at low pressure, variations in the geometry of open pore space and microfractures may enhance differences between lithologies. This consideration would imply that velocity may drop off more dramatically for porous, low-density rocks than those with a different fracture geometry. Nevertheless, despite outlying lithologies such as serpentinite and pyroxenite, previous work has indicated a broadly linear relationship between velocity and sample density for a suite of crustal lithologies across a range of pressures (e.g., Christensen & Salisbury, 1975; Ji et al., 2010, 2016).

We allow for a linear dependence of $\frac{\partial v}{\partial \rho_\circ}$ on pressure according to

$$\left(\frac{\partial v}{\partial \rho_\circ}\right)_T = d_\circ + P d_P \tag{11}$$

where $d_\circ$ is the value of $\frac{\partial v}{\partial \rho_\circ}$ at standard pressure (i.e., $P = 0.1$ MPa) and d_P is the pressure derivative of that gradient, which we assume to be constant. Finally, seismic velocity has been shown to vary approximately linearly as a function of temperature at a given pressure, such that

$$\left(\frac{\partial v}{\partial T}\right)_{P,\rho_\circ} = m \tag{12}$$

where m is a constant (e.g., Christensen & Mooney, 1995; Kern & Richter, 1981; Yamauchi & Takei, 2016). These relationships can be combined and integrated to yield a function for velocity as a function of pressure, temperature and density, $v(P, T, \rho_\circ)$, given by

$$v(P,T,\rho_\circ) = v_0 + bP + (d_\circ + d_P P)\rho_\circ + mT - c\exp(-kP) \tag{13}$$

which can be rearranged to yield sample density at s.t.p. as a function of velocity, pressure and temperature so that

$$\rho_\circ(P,T,v) = \frac{v - v_0 - bP - mT + c\exp(-kP)}{d_\circ + d_P P} \tag{14}$$

where v_0 in km s^{-1} is the extrapolated intercept velocity at $P = 0$ and $\rho_\circ = 0$ for the linear part of the relationship.

We have compiled an extensive database of laboratory measurements of seismic velocities as a function of P and $\rho_\circ$ (Figure 7). Our database includes 150 individual rock samples and covers 26 lithologies, with a total of 1,146 measurements (see Database 2 in Supporting Information S1). These experiments are all carried out at standard temperature and so cannot be used to estimate m, the temperature derivative of velocity. We exclude clear outlying exotic lithologies (e.g., kyanitite), leaving a database of 1,136 measurements of 149 samples and 25 lithologies. We use a steepest descent algorithm to optimize the other six constants in Equation 13. We minimize the misfit between measured and predicted values of $v(P, \rho_\circ)$ using

$$H = \sqrt{\frac{\sum\left(v_i^c - v_i^o\right)^2}{N}}, \tag{15}$$

where v_i^o and v_i^c are the measured and predicted velocities of the ith velocity measurement and N is the total number of data points. This optimisation procedure is performed independently for $V_P(P, \rho_\circ)$ and $V_S(P, \rho_\circ)$. Optimal values for the constants are listed in Table 2, the results for V_P are shown in Figure 8, and the equivalent figure for V_S are included in Figure S1 in Supporting Information S1.

The trade-off between these different parameters can be investigated in two complementary ways (Figure 9). First, we carry out a parameter sweep through each possible pair of parameters, while fixing the other four at the values of the global misfit minimum. Second, the covariance matrix indicates the importance of trade-offs

Table 2
Optimal Parameters for Constants in Equations 13 and 14 Obtained During Crustal Velocity-To-Density Calibration

	Parameter	Symbol	Value	Units
V_P	Intercept velocity	v_0	-0.94 ± 0.11	km s^{-1}
	$(\partial v/\partial P)_T$ for linear part of relationship	b	$(1.69 \pm 4) \times 10^{-3}$	km s^{-1} M Pa^{-1}
	$(\partial v/\partial \rho_o)_{P,T}$	d_o	2.56 ± 0.06 m^4	m^4 s^{-1} kg^{-1}
	$(\partial^2 v/\partial \rho_o \partial P)_T$	d_P	$(-4.76 \pm 1.37) \times 10^{-4}$ m^4	m^4 s^{-1} kg^{-1} MPa^{-1}
	Magnitude of exponential drop-off in v	c	1.67 ± 0.009	km s^{-1}
	Pressure lengthscale of exponential drop-off in v	k	$(1.95 \pm 0.19) \times 10^{-2}$	MPa^{-1}
	$(\partial v/\partial T)_P$	m	$(-4.0 \pm 1.0) \times 10^{-4}$	km s^{-1} K^{-1}
V_S	Intercept velocity	v_0	-0.61 ± 0.11	km s^{-1}
	$(\partial v/\partial P)_T$ for linear part of relationship	b	$(1.03 \pm 4) \times 10^{-3}$	km s^{-1} MPa^{-1}
	$(\partial v/\partial \rho_o)_{P,T}$	d_o	1.48 ± 0.06 m^4	m^4 s^{-1} kg^{-1}
	$(\partial^2 v/\partial \rho_o \partial P)_T$	d_P	$(-2.98 \pm 1.37) \times 10^{-4}$ m^4	m^4 s^{-1} kg^{-1} MPa^{-1}
	Magnitude of exponential drop-off in v	c	0.737 ± 0.009	km s^{-1}
	Pressure lengthscale of exponential drop-off in v	k	$(2.00 \pm 0.19) \times 10^{-2}$	MPa^{-1}
	$(\partial v/\partial T)_P$	m	$(-2.3 \pm 1.0) \times 10^{-4}$	km s^{-1} K^{-1}

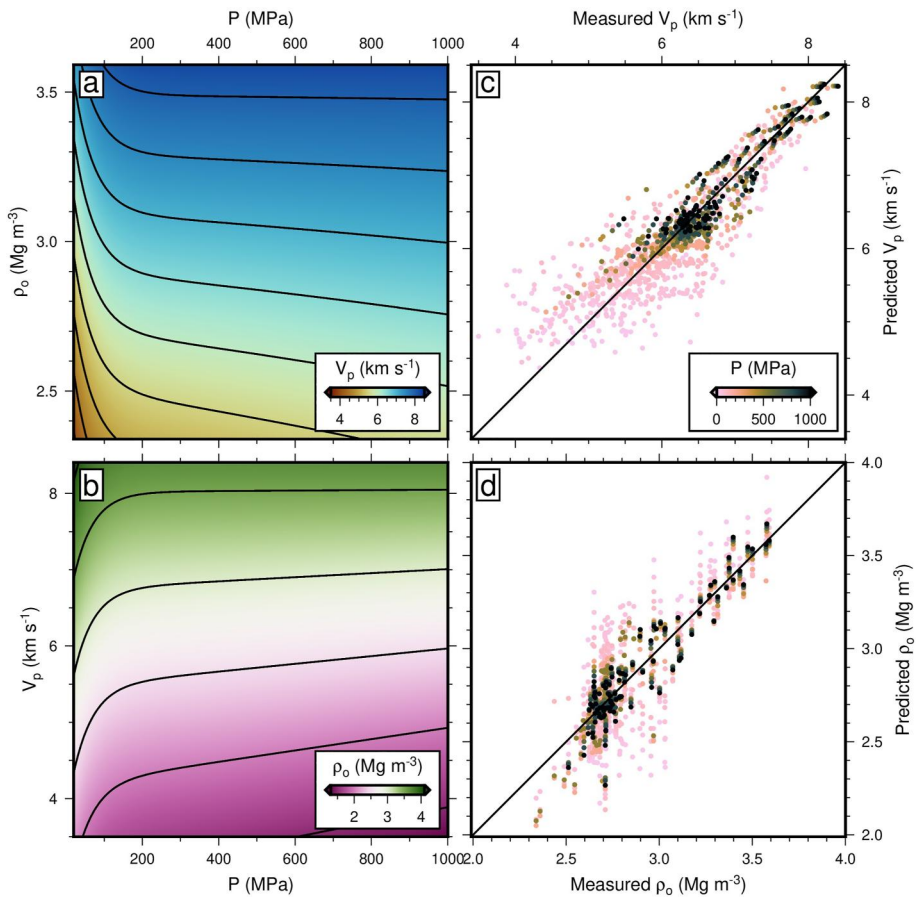

Figure 8. Seismic velocity-to-density conversion. (a) Predicted *P*-wave velocity, V_P, as a function of pressure, P, and sample density at s.t.p., ρ_o, contoured every 0.5 km s^{-1}. (b) Predicted sample density at s.t.p. as a function of pressure and *P*-wave velocity, contoured every 0.2 Mg m^{-3}. (c) Fit between measured and predicted V_P for laboratory samples from Figure 7. Black line = ideal 1:1 relationship. (d) Same for ρ_o. Note greater consistency when $P > 200$ MPa.

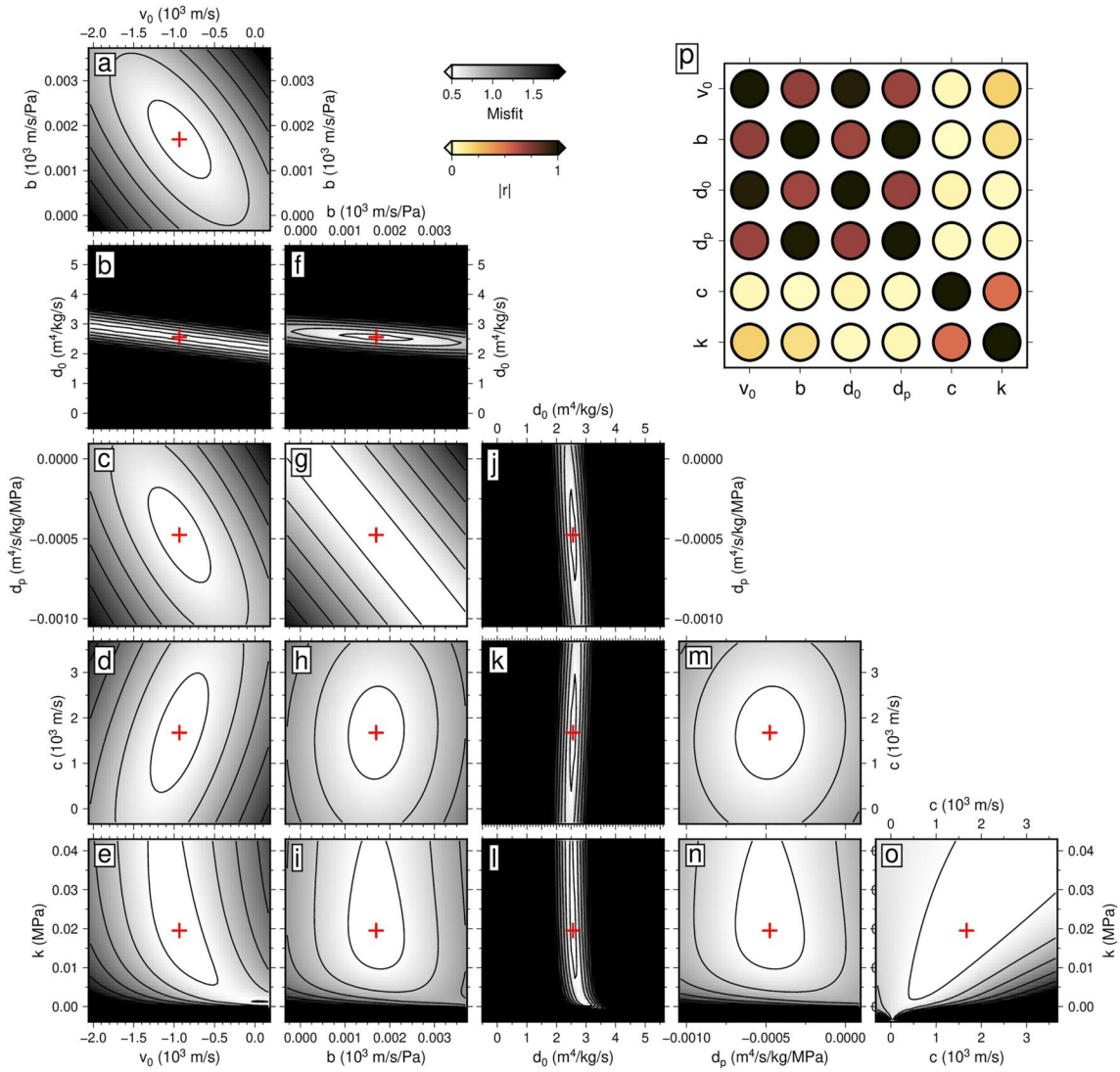

Figure 9. Trade-offs in optimal V_P-to-density conversion parameters. (a) Misfit between measured and predicted seismic velocity as a function of v_0 and b, while other parameters are held constant at the global misfit minimum. Red cross = global misfit minimum. Contours every 0.2 misfit units. Parameter values varied between ±1.2× value at global misfit minimum. (b) Same for v_0-$d_\circ$. (c) v_0-d_P. (d) v_0-c. (e) v_0-k. (f) b-$d_\circ$. (g) b-d_P. (h) b-c. (i) b-k. (j) $d_\circ$-d_P. (k) $d_\circ$-c. (l) $d_\circ$-k. (m) d_P-c. (n) d_P-k. (o) c-k. (p) Correlation matrix. Note that $|r| = 1$ along the diagonal of matrix and that correlation shown in panels (a)–(o) is not directly comparable to $|r|$ values on panel (p).

between parameter values in the vicinity of the global minimum by evaluating the Hessian matrix of the cost function using

$$\mathbf{Cov}(H) = 2\chi_\nu^2[\mathbf{Hess}(H)]^{-1} \tag{16}$$

and can be related to the degree of trade-off via the correlation matrix according to

$$\mathbf{Corr}(H) = \mathrm{diag}[\mathbf{Cov}(H)]^{-\frac{1}{2}}\,\mathbf{Cov}(H)\,\mathrm{diag}[\mathbf{Cov}(H)]^{-\frac{1}{2}}. \tag{17}$$

These two related approaches demonstrate that there are two principal groupings of parameter trade-offs. The first consists of v_0, $d_\circ$, d_P, and b, which together describe the linear component of the relationship between pressure, velocity, and density. The second occurs between c and k (and to a limited extent v_0), which are the parameters describing the exponential drop-off in velocity that occurs at low pressure. There is limited trade-off between

these two clusters of parameters. The strongest trade-off is between b and d_o, which describe the gradient of the linear component of $\frac{\partial v}{\partial P}$ and the value of $\frac{\partial v}{\partial \rho_o}$ at standard pressure, respectively. Nonetheless, our values of b, c, and k are consistent with those determined for individual samples by other studies (e.g., Ji et al., 2010, 2013; Kern & Richter, 1981).

3.2.2. Estimation of Crustal Density Profiles

To estimate crustal density as a function of depth, $\rho_{cc}(z)$, we apply our SMV2rho density conversion scheme to the published seismic velocity profiles determined from seismic refraction and receiver function analysis compiled in Section 2.2 (see SeisCruST repository; Database 1 in Supporting Information S1; Stephenson & Hoggard, 2024; Stephenson, Hoggard, Holdt, & Galbraith-Olive, 2024). First, we must return to the value of m, which captures the linear effect of temperature on seismic velocity and has been unconstrained in our analysis thus far (see Section 3.2.1). Previous studies have shown that, although values vary between samples, in general $m_{V_P} \approx -(4.0 \pm 1.0) \times 10^{-4}$ km s^{-1} K^{-1} for V_P and $m_{V_S} = -(2.3 \pm 1.0) \times 10^{-4}$ km s^{-1} K^{-1} for V_S (Christensen & Mooney, 1995; Kern & Richter, 1981). These values satisfy an assumption that the ratio V_P/V_S is constant with respect to T, so that $\frac{V_P}{V_S}\left(\frac{\partial V_S}{\partial V_P}\right)_P = 1$. Furthermore, adopting these values for m_{V_P} and m_{V_S} means that $m_{V_P}/m_{V_S} = 1.73$ is centered upon the median value and interquartile range of the database of laboratory experiments (i.e. 1.73 ± 0.04; Figure 7c; Database 2 in Supporting Information S1). It also lies within the range of values for median bulk crustal $\overline{V}_P/\overline{V}_S$ given by our database of seismic constraints on crustal structure (Database 1 in Supporting Information S1). We obtain a median value and interquartile range of 1.74 ± 0.04 by taking all locations where V_P and V_S profiles are located within 50 km of one another and 1.75 ± 0.03 by taking only bulk values for κ from H-κ stacking results (i.e., Database 1b and 1a in Supporting Information S1, respectively). Measured seismic velocities as a function of depth, $v(z)$, can therefore be corrected for the effects of temperature according to $v_c(z) = v(z) + mT(z)$. Note that treating m as a constant with respect to T essentially ignores the potential presence of anelastic effects, which generally introduce non-linearity into $\frac{\partial v}{\partial T}$ and are thought to be significant when temperatures exceed ~90% of the melting point (e.g., Yamauchi & Takei, 2016).

Second, we must estimate the likely temperature structure within the crust (i.e., $T(z)$) at the site of each seismic experiment. We parameterize the crustal geothermal gradient using a constant surface and Moho heat flux and an exponentially decreasing internal heat generation with depth so that

$$T(z) = T_0 + \frac{q_m z}{k} + \frac{(q_0 - q_m)\, h_r}{k}\left[1 - \exp\left(\frac{-z}{h_r}\right)\right], \tag{18}$$

where $T_0 = 10$°C is the temperature at the surface, $q_0 = 59 \pm 14$ m W m^{-2} and $q_m = 30 \pm 10$ m W m^{-2} are the surface and Moho heat flux, respectively, $h_r = 10$ km is a characteristic length scale describing the rate of decrease of internal heat production with depth, and $k = 2.5$ W m^{-1} K^{-1} is the thermal conductivity. Pressure as a function of depth, $P(z)$, can be calculated by integrating the overburden density with respect to depth using

$$P(z) = g \int_0^z \rho_{cc}(z)\, \mathrm{d}z. \tag{19}$$

Combining $v_c(z)$ with Equations 14 and 19 permits calculation of the density of a package of crustal rock from any depth as if it were at s.t.p. (i.e., we can estimate $\rho_o(z)$ using an observed value of $v(z)$ from the seismic experiment). Since we are interested in the rock's actual density at depth, $\rho_{cc}(z)$, we must subsequently account for the effects of pressure and temperature on ρ_o using Equation 5, but substitute in appropriate values for crustal rocks of $\alpha_0 = 1.0 \times 10^{-5}$ K^{-1}, $\alpha_1 = 2.9 \times 10^{-8}$ K^{-2}, and bulk modulus, $K_{cc} = 90$ GPa (Cooper & Simmons, 1977; Kern & Richter, 1981; Schrank et al., 2012). We note that α also varies as a function of P and that K_{cc} also varies as a function of P, T, and ρ, (e.g., Kern & Richter, 1981), but have ignored this additional complexity here.

Of the localities within our crustal thickness database excluding Greenland and Antarctica, 4,067 have accompanying seismic velocity profiles and we use these $V_P(z)$ and $V_S(z)$ measurements to estimate crustal density as a function of depth (Figure 10; Stephenson & Hoggard, 2024). There is a general increase in seismic velocity with depth, which yields a corresponding increase in density with depth. There is also a substantial spread in velocities

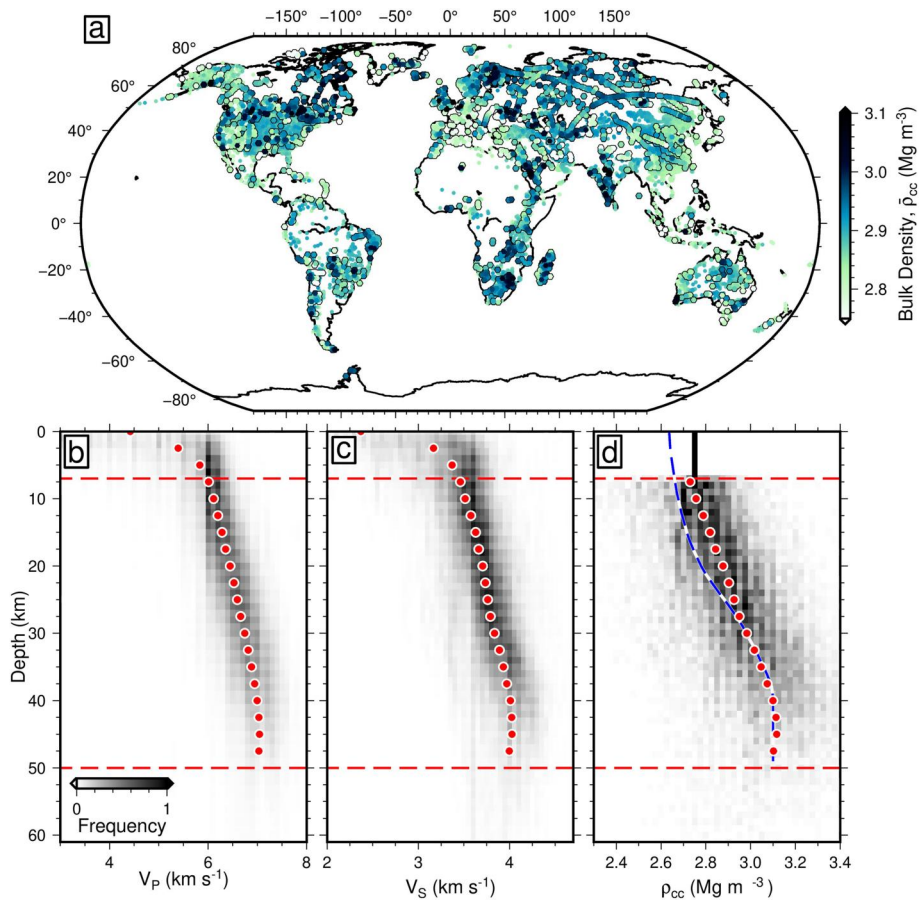

Figure 10. Crustal velocity and density profiles. (a) Bulk crustal density at all sites plotted using a Robinson projection. Hexagons with black outlines = locations where seismic velocity profiles were directly used to constrain bulk density. Open circles = locations where density was calculated using relationship between average bulk density and crustal thickness (Equation 21). (b) Stacked global V_P profiles. Dashed red lines = minimum/maximum depth bounds over which crustal velocity-to-density scheme is applied; red circles = mean values. (c) Same for V_S profiles. (d) Stacked global crustal density profiles calculated by converting V_P and V_S profiles into density. Red circles = mean density as a function of depth; dashed blue line = average crustal depth-density relationship from Christensen and Mooney (1995).

at shallow depths (Figures 10b and 10c), which when converted into density using our generalized scheme, results in an unrealistically large range of ρ_{cc} values in the uppermost crust. At low pressure, the laboratory analyses show that the exponential poro-elastic component of the $\frac{\partial v}{\partial P}$ relationship starts to dominate and can be quite variable between different samples, which reduces the reliability of our density conversion scheme where $P < 200$ MPa (e.g., Ji et al., 2010). Due to this strong and unpredictable lithologic variation, the effect of this exponential velocity drop off is very difficult to generalize. Furthermore, shallow seismic velocities are not particularly well resolved using seismic imaging techniques such as inverse modeling of surface waves, meaning that an exponential velocity decay is often not imaged in 1D velocity profiles. We have therefore chosen to fix a constant value of $\overline{\rho}_{cc} = 2.75$ Mg m^{-3} within the upper 7 km of each profile. In the case that a deep sedimentary basin of density 2.65 Mg m^{-3} occupies this uppermost 7 km, then it is possible to show using Equation 8 that we would underestimate topography by ∼200 m. Conversely, if the uppermost 7 km is composed of mafic intrusions and lava flows, then density could be 2.95 Mg m^{-3} and topography overestimated by up to ∼300 m. These situations are nonetheless likely to represent extreme cases and the true local value of ρ_{cc} in the uppermost 7 km will be closer to our assumed value.

This approach is only fully applicable to the 3,969 localities with a $V_P(z)$ or $V_S(z)$ profile. However, the superior geographic distribution of crustal thickness estimates provided by techniques such as H-κ and common conversion point (CCP) stacking of receiver functions means that it would be beneficial to also estimate bulk crustal

density at the site of those experiments. H-κ stacking yields an estimation of the bulk V_P/V_S ratio of the crust, and several previous studies have used this value to approximate crustal density. It does not appear, however, that the $\overline{V}_P/\overline{V}_S$ ratio provides a sufficiently accurate constraint for our purposes since it is relatively invariant across a range of lithologies, ρ_o, P, and T values (see Figure 7c). Instead, we can exploit the fact that there is a degree of correlation between depth and density in Figure 10d, such that the local crustal thickness obtained from, for example, H-κ or CCP stacking serves as a better guide to the mean crustal density.

For all localities that do have a $V_P(z)$ or $V_S(z)$ profile, we can calculate the mean crustal density as a function of depth (red dots in Figure 10d) and approximate it using the best-fitting third-order polynomial function given by

$$\rho_{cc}(z) \approx 2.75 - \left(5.20 \times 10^{-3}\right) z + \left(7.62 \times 10^{-4}\right) z^2 - \left(1.00 \times 10^{-5}\right) z^3 \tag{20}$$

We can also use these locations to construct a bulk density curve as a function of crustal thickness, $\overline{\rho}_{cc}(t_{cc})$, which can be approximated using

$$\overline{\rho}_{cc}(t_{cc}) \approx 2.75 - \left(2.73 \times 10^{-3}\right) t_{cc} + \left(2.52 \times 10^{-4}\right) t_{cc}^2 - \left(2.56 \times 10^{-6}\right) t_{cc}^3 \tag{21}$$

Both of these relationships are most reliable over the range 7–50 km for both z and t_{cc} (see Section S5 in Supporting Information S1). Across our entire database, we obtain a mean value for bulk density of the continental crust of 2.88 ± 0.05 Mg m^{-3}. We note that this value is consistent with the range of 2.89 ± 0.29 Mg m^{-3} determined by the simple linear regression of crustal thickness against elevation in Section 3.1, but has substantially smaller variance.

3.2.3. Limitations, Assumptions, and Uncertainties

In order to gain an intuitive understanding of where our velocity-to-density conversion scheme is likely to be more (or less) reliable, it is important to re-emphasize the assumptions and simplifications that we have made. First, in Equation 18, we have implicitly assumed that Moho temperatures are correlated with crustal thickness. The value of q_m is especially poorly constrained, while q_0 is both noisy and only patchily measured (see, e.g. J. H. Davies & Davies, 2010). In other words, variations in Moho heat flux caused by lithospheric and asthenospheric mantle structure will be manifest in our results as errors in crustal density. Consider a column of continental crust that is 40 km thick, where the temperature at the Moho for our reference values of q_m and q_0 will be about 600°C. If q_m and q_0 were increased to 50 and 80 mW m^{-2}, respectively, then the temperature at the Moho would increase to ∼930°C. The higher temperature will decrease V_P by 0.14 km s^{-1}, which after correcting for this velocity decrease, will lead to an increase in ρ_o of 0.07 Mg m^{-3} at a depth of 40 km relative to a situation in which we did not account for T. However, the extra thermal expansion would reduce density by 0.04 Mg m^{-3}, resulting in a net density difference of only ∼+0.03 Mg m^{-3} between regions with high and more normal geothermal gradients. It is important to bear in mind that this density difference becomes smaller as temperature decreases, meaning that when estimating the average value for the bulk crust, this correction will be smaller still, in this case ∼+0.01 Mg m^{-3}. This uncertainty maps into an uncertainty in topographic elevation of only ±∼120 m for crust of average thickness (i.e., 39.7 km). Compare this value to a change in bulk crustal density of 0.11 Mg m^{-3} caused by a reasonable difference in bulk $\overline{V}_P$ of ±0.3 km s^{-1} (i.e., 1σ variation in global bulk V_P in the crustal database), which maps into 1.35 km of elevation difference. From this comparison, it is clear that lithologic controls on the relationship between v and ρ_o are the most important consideration and that realistic uncertainties in the absolute value of T are of secondary concern. Nonetheless, since P and T generally increase with depth, it is important to not entirely neglect their effect if we are to avoid introducing larger, systematic biases into bulk crustal density estimates (e.g., Christensen & Mooney, 1995).

Second, we have not accounted for changes in K_{cc} or m as a function of P and T, or variations in α as a function of P. If K_{cc} varied by ±50 GPa, then ρ at a depth of 40 km would vary by $^{+0.04}_{-0.01}$Mg m^{-3}. Similarly, if both α_0 and α_1 were varied by ±50% then ρ_o at a depth of 40 km would vary by ±0.02 Mg m^{-3}. We consider these parameter ranges to represent extreme cases given their published values (Cooper & Simmons, 1977; Ji et al., 2009; Schrank et al., 2012). We formally propagate uncertainties in all parameters through our density calculation in Section S4 in Supporting Information S1.

Despite the generally limited impact of uncertainty in these parameter values upon estimated density, there are localized circumstances in which the uncertainties could be larger. We have mostly neglected the anelastic and poro-elastic effects of high homologous temperatures, as well as the potential presence of water and/or melt on seismic velocities. For example, we exclude certain lithologies such as serpentinite, which can have a lower seismic velocity relative to its density due to greater water content, and have not fully accounted for the significant decrease in $\overline{\rho}_{cc}$ that is associated with the opening of pore space at low pressure in sedimentary rocks (Ji et al., 2013; Wyllie et al., 1956). These simplifications will have locally important effects upon absolute values of crustal density, particularly at shallow depths (i.e., $\lesssim$7 km) or in regions with very high temperatures (e.g., either thick crust with high radiogenic heat content, thin crust with high basal heat flow, and/or presence of melt). Finally, we ignore the $\alpha \rightarrow \beta$ spin transition in quartz that occurs at about 570°C at surface pressures and thereafter at progressively higher temperatures (i.e., 0.255°C MPa^{-1}; Ohno, 1995; Johnson et al., 2021). This transition causes a rapid drop in V_P, V_S, and K_{cc}, followed by a subsequent rebound to markedly higher values (Ohno, 1995). It is only likely to be encountered, however, in places with significantly elevated geothermal gradients.

To summarize, since the majority of locations are not significantly affected by highly elevated geothermal gradients, melt, or uncommon lithologies, our density conversion scheme should be broadly applicable to the majority of continental settings. The most important predictor of crustal density is seismic velocity, with other considerations being secondary controls (e.g., Levandowski et al., 2014). We therefore anticipate that these assumptions will have limited impact on global trends in bulk crustal density and residual topography. Finally, existing density models often subdivide the crust into a number of layers of constant density (e.g., `Crust1.0`; Laske et al., 2013), whereas any discontinuities present in our density inference must be inherited directly from the local velocity profile. Ascertaining whether this alternative approach permits detailed mapping of internal layering will require further work.

3.3. Choice of Reference Crustal Column

In order to estimate continental residual topography, it is necessary to define a reference column against which observed crustal buoyancy structure can be compared (Figure 6). For this purpose, we exploit the structure of continental crust at sea level. This choice contains an implicit assumption that the residual topography for all continental crust whose surface is at sea level averages to zero. The thickness of this crust in our reference column, $t_{cr} = 32.1$ km, is calculated by averaging crustal thickness measurements at all 884 locations within our database that lie within ±25 m of sea level (see Section S3 in Supporting Information S1). This value is 7.6 km thinner than the global average crustal thickness value, which includes mountainous and otherwise excised regions. The average bulk density of this reference column, $\overline{\rho}_{cr} = 2.84$ Mg m^{-3}, is calculated by taking the median of our bulk crustal density estimates at these locations (see Section S3 in Supporting Information S1). The median values of t_{cr} and $\overline{\rho}_{cr}$ do not differ significantly from their mean.

It is important to acknowledge that alternative reference columns can be adopted and are equally valid. For example, the mid-oceanic ridge is often exploited as the reference template since its density structure is relatively simple and well known (e.g., McNab et al., 2018; Wang et al., 2022). Nevertheless, a significant advantage of our approach is that it exploits continental crust on both sides of the isostatic balance and is therefore self-consistent, mitigating systematic uncertainties in lithospheric structure and composition between oceanic and continental settings and allowing us to focus on random uncertainties. For example, variations in the geothermal gradient and values of the bulk modulus and m are minimized by using a continental reference, since these potentially systematic uncertainties appear on both sides of the isostatic balance. It is also important to note that we have not thus far accounted for isostatic topography specifically generated by the lithospheric mantle. This omission means that our estimates of continental residual topography include topography generated by buoyancy at any depth within the mantle (i.e., from all depths beneath the Moho, inclusive of the lithospheric mantle). This approach means that, in effect (and subject to differences in reference column) our residual topographic estimates would be an appropriate proxy for dynamic topography as defined by Forte et al. (1993) and Forte and Rowley (2022), but do not meet the definition of Molnar et al. (2015). The use of a continental reference column and omission of a correction for lithospheric isostasy means that our residual topographic results will be similar, though not directly comparable, to oceanic residual bathymetric estimates that account for the first-order effect of plate cooling (Hoggard et al., 2017; Holdt et al., 2022; Winterbourne et al., 2014).

3.4. Propagation of Uncertainties Into Estimates of Residual Topography

The parameters involved in the isostatic corrections of Equations 2 and 8 can have significant uncertainties that must be propagated into uncertainties in residual topography, σ_{e_r}. We propagate errors assuming these parameter uncertainties are uncorrelated with one another and that the uncertainty in measured elevation is essentially zero for our purposes. The full procedure is summarized here and described in full in Section S4 in Supporting Information S1. Since the reference column is the same for all datapoints, its uncertainty is systematic (i.e., all residual topographic estimates shift upwards or downwards by a constant value) and so can be neglected in this analysis. First, we estimate uncertainties in $\overline{\rho}_{cc}$ by employing a *Monte Carlo* strategy to propagate errors through our density conversion algorithm. Next, we analytically propagate these uncertainty values through the residual topographic calculation, incorporating uncertainties in other density and thickness parameters (Section S4 in Supporting Information S1). We find that uncertainties in residual topographic anomalies depend most significantly on the uncertainty in $\overline{\rho}_{cc}$, which in turn is a function of the method used to measure crustal thickness and seismic velocity. The absolute value of t_{cc} plays an important secondary role in determining uncertainty, with uncertainty in residual elevation scaling with increasing crustal thickness. For example, for a V_P profile with $t_{cc} \lesssim 30$ km, then the uncertainty $\sigma_{e_r} \lesssim 1.0$ km, but it increases for larger values of t_{cc}. Corresponding uncertainty values are greater for densities derived from V_S and for those locations with no velocity profile at all. The slope of the relationship between σ_{e_r} and t_{cc} depends strongly upon the uncertainty in crustal density. Note that these uncertainty estimates are indicative for an individual velocity profile, but they are reduced when multiple seismic experiments have imaged the same region of crust and return consistent values, assuming errors in different studies are random and uncorrelated.

3.5. Flexural Effects, Ice Loading, and Geoid Height Correction

Surface and internal loads, such as those generated by orogenesis, volcanic emplacement, sedimentary deposition and glacial loading, can generate significant amplitudes of flexural topography. This topography is not in isostatic equilibrium and is generally also associated with high-amplitude free-air gravity anomalies. Lithospheric flexural rigidity determines the lengthscale of deformation generated by this loading, the value of which is thought to vary significantly within the continental realm and has been the subject of both significant research and controversy (e.g., Audet, 2014; D. McKenzie & Fairhead, 1997; Tesauro et al., 2012; Watts & Burov, 2003). In order to sidestep this issue, we excise from the database any regions that have experienced significant Cenozoic orogenesis using the exclusion polygons of Hoggard et al. (2016) and Holdt et al. (2022). This approach excludes the Himalaya-Tibet, Tien Shan, and Zagros mountain belts. Also excluded are the Andes, Atlas, European, Japanese, and Southern Alps, Apennines, Balkans, and Carpathians.

While it is possible to correct for ice loading, we have excluded regions covered by present-day ice sheets owing to the increase in uncertainty related to estimating ice thickness. Nevertheless, we do include regions that are not currently covered by ice but were formally affected by glaciation during the Last Glacial Maximum, such as Fennoscandia, northern North America and the British Isles. Whilst these regions are still yet to attain full isostatic equilibrium, their current displacement from equilibrium is substantially smaller than amplitudes of residual topography. For example, by fitting a simple exponential decay to the elevations of dated raised beach deposits around Hudson Bay (i.e., near to the center of the former Laurentide Ice Sheet), Peltier (1994) showed that the amount of relative sea-level fall yet to take place is 10–100 m. Similarly, in locations of ongoing forebulge collapse, the amount of relative sea-level rise yet to take place is only around 10 m.

Finally, it should also be noted that throughout this study, we use local mean sea level as our elevation reference datum, which coincides with the gravitational equipotential surface (i.e., the geoid). Since the geoid itself is regionally deflected away from hydrostatic equilibrium by up to ∼100 m as a result of processes such as mantle convection, it may be appropriate in some circumstances to implement a correction for variations in the height of the non-hydrostatic surface (i.e., to reference residual topographic anomalies to the hydrostatic equilibrium figure; e.g. Chambat et al., 2010). The following analyses do not require any such reference-frame correction and so we do not apply one here. We emphasize, however, that it may be necessary to apply such a correction if one wishes to compare our results to certain numerical predictions of dynamic topography that are referenced to the hydrostatic figure (see, e.g. Hoggard et al., 2017; Holdt et al., 2022).

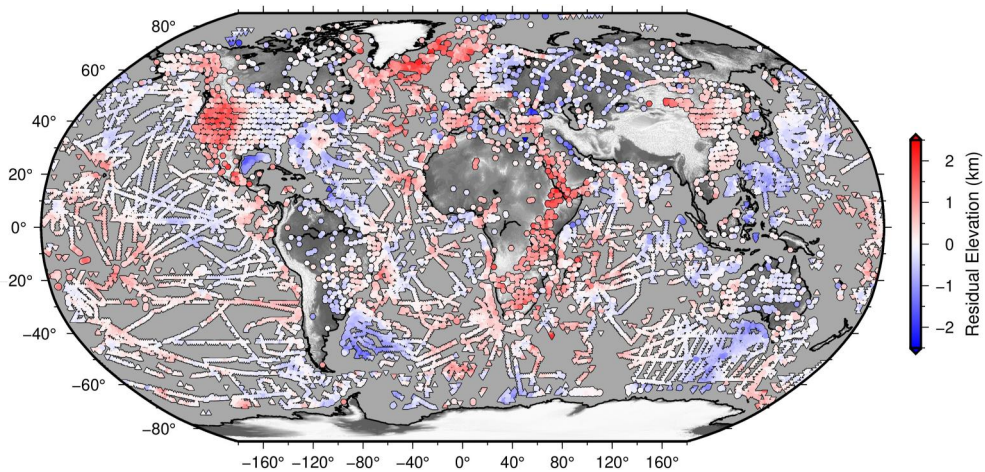

Figure 11. Global residual topography and bathymetry. Hexagons = mean air-loaded onshore residual topographic estimates (after correcting for crustal isostasy), averaged into 2° × 2° bins on Robinson projection; circles = most accurate water-loaded oceanic residual depth estimates from Holdt et al. (2022); up/down triangles = minimum/maximum oceanic residual depth estimates, where crustal thickness is only regionally constrained. Note that oceanic residual depth estimates have been corrected for the effect of plate cooling (see Section 3.3).

4. Global Residual Topography

We present a new database of global residual topographic estimates that have been calculated by correcting for crustal thickness and density variations (Figure 11; Database 3 in Supporting Information S1). These residual topographic estimates can be interpreted as a best estimate of the amplitude of topography that is generated and supported by the whole range of sub-crustal processes. Our results are averaged into 1°, 2°, 3°, and 4° bins. Our reason for binning e_r estimates is threefold. First, our study is a global analysis, exploiting hundreds of disparate individual seismic imaging studies that encompass a wide range of techniques and assumptions to determine crustal structure. We wish to combine these results in a self-consistent manner. In calculating e_r, we have carefully estimated the magnitude of uncertainties associated with each estimate and in some, but not all, cases, these uncertainties are relatively large. Our aim here is to elucidate spatial variations in e_r by combining estimates within a given geographic area into a single, weighted average value, $\overline{e}_r$, while representing the variance in that average value, $\sigma^2_{\overline{e}_r}$. For this reason, we weight each residual topographic estimate by the inverse of its variance such that the weight of the ith residual topographic estimate is given by $w_i = 1/\sigma_i^2$. The average value within each bin is given by

$$\overline{e}_r = \frac{\sum_{i=1}^{n} w_i e_{r_i}}{\sum_{i=1}^{n} w_i}, \tag{22}$$

and the standard error on $\overline{e}_r$ is given by

$$\sigma_{\overline{e}_r} = \left\{ \sum_{i=1}^{n} \frac{1}{w_i} \right\}^{-\frac{1}{2}}. \tag{23}$$

In this way, the mean and variance of the residual topographic value within each bin is representative of the combined mean and variance of the contributing datapoints. Our second reason for carrying out geographic binning is to average local effects that may not be taken into account within our analysis. Such considerations may include locally more exotic crustal lithologies or random errors associated with seismic imaging experiments. Finally, flexural effects can be mitigated if spot measurements are averaged over distances that exceed the flexural wavelength (Section 3.5).

Following this procedure, we calculate spatially averaged residual topography for all locations where $15 < t_{cc} < 50$ km (Figure 11). The mean and standard deviation of the 2-degree binned database is +250 ± 560 m

and the median value is +180 m. It is important to note that this minor bias toward positive residual topography is to be expected, since we have only included onshore seismic experiments in our crustal database. Thus localities where, for example, crustal thickness is 20 km and $\overline{\rho}_{cc}$ is equal to ρ_{cr} require a residual topographic anomaly of ∼+1.5 km for the surface to be at sea level. This consideration means that the majority of sites that have thin crust, yet are located at or above sea level, must be associated with positive residual topographic anomalies to be observed onshore. Indeed residual topographic estimates in locations where $t_{cc} \lesssim 30.0$ km form an increasingly one-tailed distribution that is skewed toward positive values. Conversely, for locations with $40 < t_{cc} < 50$ km, the distribution of residual topography is more normally distributed with a mean value of only -10 ± 580 m and a median of −100 m.

The largest positive residual topography anomalies are located in the Afar-Yemen-Red Sea region, western North America, and Iceland, where amplitudes reach ∼+2 km. Other significant positive excursions occur in southern Africa, along the length of the East African Rift, in Madagascar, Anatolia, Iberia, and east Asia. The largest negative anomalies occur in regions surrounding the Black, Caspian, and Aral Seas, as well as a large portion of the bordering East European Plain, although we note that e_r is more uncertain and noisy here. In this region, residual topography peaks at deeper than −1.5 km. Other significant negative excursions occur in the eastern United States, central Canada, southern Brazil and around the Baltic Sea. Lateral gradients in residual topography peak at ∼2 m km^{-1}.

These patterns of residual topography are clearly spatially coherent and exceed both the length scale of lithospheric flexure and uncertainties in the amplitude of residual topographic estimates. It is therefore likely that they reflect the buoyancy structure of the underlying mantle. Detailed spectral analyses of these anomalies were recently carried out by Holdt et al. (2022), who demonstrated that the power spectrum can be explained by sub-plate mantle structure out to spherical harmonic degree 40 (i.e., wavelengths down to ∼1,000 km). Here, rather than further explore these spectral characteristics, we instead investigate qualitative relationships between residual topographic anomalies and other geological and geophysical observations. Data sets that we interrogate include oceanic residual bathymetric anomalies, elevations of marine sedimentary rocks, sites of major denudation and/or intraplate magmatism, gravity anomalies, and seismic velocities within the upper mantle.

First, we compare our estimates of residual topography to a number of independent global data sets that provide constraints on both sub-crustal and sub-plate support. There is a weak positive correlation ($r = 0.38$) between long-wavelength free-air gravity anomalies, which are sometimes used as a crude proxy for sub-plate support, and our estimates of residual topography (Figure 12a; Colli et al., 2016; Ebinger et al., 1989; Hoggard et al., 2016; D. McKenzie & Fairhead, 1997; Molnar et al., 2015). The slope of the best-fitting relationship implies an admittance at long wavelengths between free-air gravity and topography of $Z = \delta g_{FA}/e_r = 61 \pm 5.5$ mGal km^{-1}. Since seismic velocities within the shallow mantle are often treated as a proxy for mantle temperature, slow velocities and high temperatures are expected beneath regions of positive residual topography (Hoggard et al., 2017; Priestley & McKenzie, 2006; Richards et al., 2020; Yamauchi & Takei, 2016). There is a corresponding negative correlation ($r = -0.52$) between shear-wave velocities averaged between 150 ± 25 km depth and residual topography (Figure 12b). The youngest age of marine sedimentary cover indicates the most recent time that continental interiors were inundated and therefore places a backstop on the amplitude and timing of uplift events. Fernandes and Roberts (2021) compiled a large database of paleobiological assemblages from previously published studies, which they used to estimate the magnitude of uplift required to place a given fossil assemblage at its modern-day elevation. This procedure requires first correcting for paleowater depth at the time of deposition of each assemblage, and second for the compaction effects of burial and exhumation. In this way a database of spot estimates of time-integrated uplift since the deposition of each fossil assemblage was assembled. We observe a positive correlation ($r = 0.54$) between the magnitude of uplift implied by the elevation of marine sedimentary rocks deposited between the start of the Cretaceous and the end of the Neogene periods and the magnitude of residual topography (Figure 12c). Finally, Ball et al. (2021) presented a global database of the locations of intraplate magmatic provinces. Almost every site (i.e., 95%) of intraplate magmatism that was active within the last 10 Ma is associated with positive residual topography. The median value of residual topographic estimates located within 2 arc degrees of a site of intraplate magmatism is >500 m greater than the global median value. These observations indicate that sub-crustal and sub-plate processes are likely contributing to the generation of residual topography, and that in many cases, this residual topography has been generated on short timescales. We can now scrutinize these relationships in more detail by examining a series of regional transects.

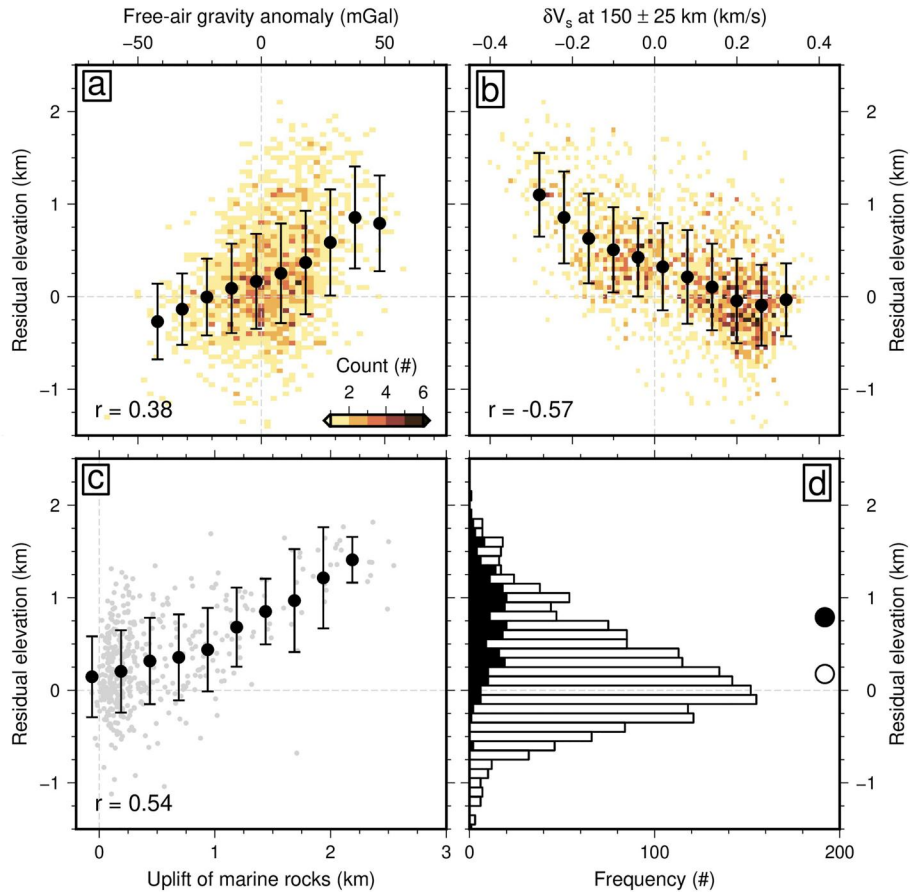

Figure 12. Comparisons between residual topographic estimates and independent data sets. (a) Residual topography as a function of long-wavelength free-air gravity anomalies, δg_{FA}, low-pass filtered for wavelengths >730 km. Color scale = count of 2° geographically binned residual topographic estimates within 2.5 mGal × 0.05 km grid cells. Black circles with error bars = running mean and standard deviation at 10 mGal intervals using boxcar weighting function of width 20 mGal. Light gray dashed lines indicate where $e_r = 0$ and gravity anomaly = 0. Pearson's rank correlation coefficient, $r = 0.38$. Equation of best-fitting relationship using orthogonal distance regression $\delta g_{FA} = (61 \pm 5.5)e_r - (27.5 \pm 3.2)$. (b) Residual topography as a function of shear-wave velocity anomaly, δV_S, averaged over a depth range of 150 ± 25 km, from the SL2013sv tomography model (Schaeffer & Lebedev, 2013). Color scale = count of 2° geographically binned residual topographic estimates within 0.01 km s^{-1} × 0.05 km grid cells. Running mean and standard deviation calculated at 0.06 km s^{-1} intervals with boxcar weighting function of width 0.06 km s^{-1}. Pearson's rank correlation coefficient, $r = -0.57$. Equation of best-fitting relationship $\delta V_S = (-0.18 \pm 0.01)e_r + (0.12 \pm 0.007)$. (c) Residual topography as a function of uplift implied by elevation of Cretaceous-to-Neogene (i.e., 145–2.3 Ma) marine rocks Fernandes and Roberts (2021). Gray circles = average elevation of marine rocks within 2 arc degrees of each 2° binned residual topographic estimate. Black circles with error bars = running mean and standard deviation at 0.25 km intervals using boxcar weighting function of width 0.5 km. Equation of best-fit relationship $U = (1.1 \pm 0.1)e_r + (0.1 \pm 0.01)$. Pearson's rank correlation coefficient, $r = 0.54$. (d) Frequency of 2° geographically binned residual topographic estimates in 0.1 km bins. White bars = whole database; black bars = locations within 2 arc-degrees of intraplate magmatic province that are ≤10 Ma (Ball et al., 2021); white circle = median residual topography of whole data set; black circle = median residual topography of locations within 2 arc-degrees of intraplate magmatic province.

4.1. North America

The spatial density of residual topographic constraints for North America reveals a well-resolved swell along the western seaboard (Figure 13). This swell is centered on the Colorado Plateau, where its peak amplitude is ~2 km. To the north, the amplitude of the anomaly decreases to ~1 km into the Northern Rocky Mountains and Cascades. To the south, its amplitude is maintained onto the Mexican Altiplano. The eastern extent of the swell coincides approximately with the western edge of the Great Plains, where its amplitude decreases to between neutral values and approximately −1 km. On the continental margins, our onshore residual topographic anomalies broadly correspond with previously estimated values of residual bathymetry in the oceanic realm, albeit that they are air-

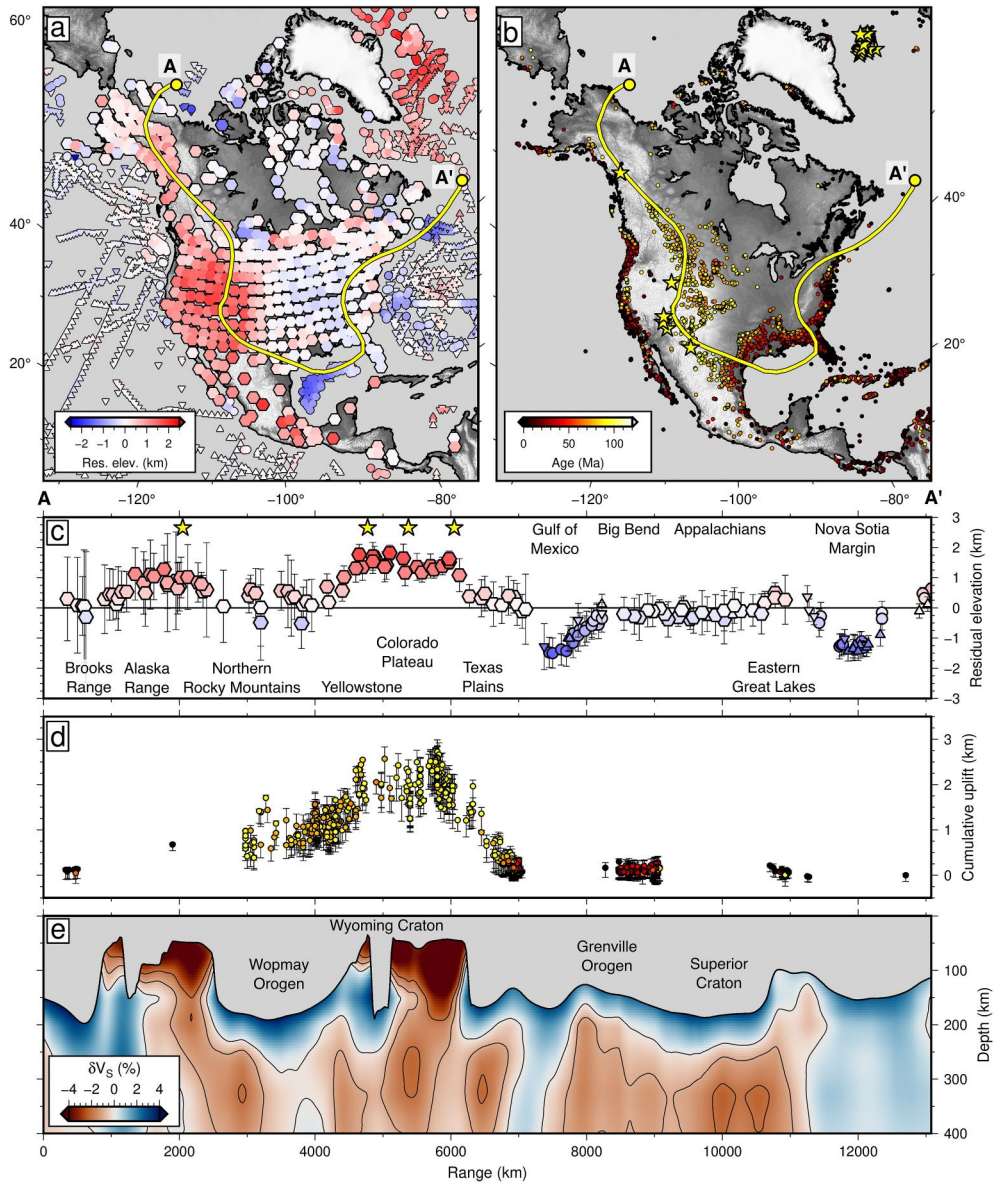

Figure 13. Relationship between residual topography and other data sets in North America. (a) Hexagons = onshore residual topographic estimates (after correcting for crustal isostasy), averaged over 1° bins. Circles = most accurate oceanic residual depth estimates; up/down triangles = minimum/maximum oceanic residual depth estimates, where crustal thickness is gauged from regional constraints alone (Hoggard et al., 2017; Holdt et al., 2022). Yellow line = location of transect. (b) Circles = location of Cretaceous-to-Recent marine fauna used to estimate cumulative uplift (Fernandes & Roberts, 2021); yellow stars = location of ≤10 Ma intraplate mafic magmatism Klöcking et al. (2018), Ball et al. (2021). (c) Northwest-to-east transect showing residual topography within a 300 km-wide swathe, symbols as before. (d) Elevation of Cretaceous-to-Recent marine fauna within 200 km-wide swathe of transect path. (e) Vertical slice through SL2013sv shear-wave tomographic model (Schaeffer & Lebedev, 2013). Gray shading = approximate depth to base of lithospheric plate (Hoggard, Czarnota, et al., 2020; Schaeffer & Lebedev, 2013).

loaded rather than water-loaded (Hoggard et al., 2016, 2017; Holdt et al., 2022; Winterbourne et al., 2014). For example, around the northern coast of the Gulf of Mexico, residual topographic anomalies decrease toward a previously documented −1.8 km residual bathymetric depression. Similarly, the amplitude of residual depth anomalies along the eastern margin corresponds with neutral residual topography onshore. An exception is found on the western coast of California, where weakly negative oceanic residual bathymetry sits beside positive residual topography. A similar juxtaposition occurs between central Mexico and the Gulf of Mexico.

The timing of growth of this swell can be explored by examining present-day elevation and age of marine stratigraphy across the region. The Mancos Shale, which crops out predominantly in Colorado, Utah, Arizona, Wyoming, and New Mexico, was deposited during Cenomanian to Campanian times. It hosts a variety of marine fauna including ammonites, mesosaurs and sharks, indicative of a shallow marine environment (e.g., Cumbaa et al., 2010; Kaufmann, 1977). At present, this formation sits on the Colorado Plateau at elevations of ∼2 km above sea level (e.g., Sahagian, 1987). The locus of these uplifted marine rocks coincides with the center of the large western North American swell, as manifest in our new residual topographic estimates (Figure 13d). Furthermore, the amplitude of the swell is in close agreement with the maximum uplift recorded by the fossil assemblages (Fernandes & Roberts, 2021). This relationship suggests that the majority of the swell developed since Cretaceous times. Indeed, calibrated analysis of drainage networks has suggested that this swell grew rapidly during Cenozoic times and is accompanied by a pulse of denudation and sedimentary flux to the neighboring margins (Fernandes et al., 2019; Galloway et al., 2011; Karlstrom et al., 2008; Roberts et al., 2012; Stephenson et al., 2014).

Intraplate mafic magmatism has occurred in western North America since Late Cretaceous times, with a substantial increase in magmatic activity during Neogene times. Magmatism has been shown to be associated with an anomalously thin lithospheric plate and, in places, a higher than ambient asthenospheric potential temperature (Klöcking et al., 2020; Plank & Forsyth, 2016). Both of these conditions are expected to give rise to positive residual topography. Indeed, magmatism clearly coincides with the broad western North American swell.

Finally, the presence of a region of slow seismic velocities within the upper mantle beneath western North America and fast anomalies beneath eastern North America suggests that the lithosphere is significantly thicker beneath the east than the west (Figure 13e; Hoggard, Czarnota, et al., 2020; Hopper & Fischer, 2018; Schaeffer & Lebedev, 2014; Sigloch, 2011). This architecture is corroborated by significantly higher geothermal heat flow in the west compared to the east (e.g., Blackwell et al., 2006). Taken together, these observations indicate the presence of significantly thinner lithosphere and hotter asthenosphere in the west, which is manifest at the surface as a significant topographic swell (Bird, 1979; Klöcking et al., 2018; Levander et al., 2011). Numerical simulations have previously suggested that this swell could be partly maintained by sub-crustal mantle flow (e.g., L. Liu & Gurnis, 2010; Moucha et al., 2009).

4.2. Eurasia

In Figure 14, we present a transect from Iceland to Japan. In a region encompassing Iceland, residual topographic estimates corroborate the existence of a major swell with an amplitude of up to ∼2 km. A wide range of well-documented evidence suggests that Iceland is underlain by a significant mantle plume (e.g., Matthews et al., 2016; Rickers et al., 2013; Schilling, 1973; White et al., 1992). In this region, onshore residual topography is in close agreement with offshore residual bathymetry (Hoggard et al., 2017; Holdt et al., 2022). The British Isles are characterized by residual topography of +0.1–1.0 km. This region is likely to be influenced by the Icelandic Plume, since anomalously slow shear wave anomalies extend beneath the British Isles (Davis et al., 2012; Rickers et al., 2013; Schoonman et al., 2017). Inverse modeling of seismic velocities in shelfal sediments and onshore thermochronologic studies have revealed a significant pulse of Cenozoic denudation that possibly extended into Neogene times (Davis et al., 2012; Holford et al., 2010; Mackay & White, 2006). We note that this regional extent of the Icelandic Plume is corroborated by our measurements, with elevated continental margins extending from Norway to the coast of mainland Europe that closely correspond with the spatial extent of oceanic residual depth, free-air gravity, and shear wave velocity anomalies.

The European Cenozoic Rift System is characterized by neutral to ∼+1 km residual topographic anomalies. In the Rhine, Limagne, and Eger Grabens, tectonic extension has occurred from Neogene-to-Recent times and contemporaneous magmatism is present in the volcanic Eifel and Massif Central provinces (e.g., Ball et al., 2021; Houtgast & Van Balen, 2000). Modeling of gravity anomalies, heat flow, passive, and active seismic data, and the composition of mafic magmatic rocks indicate that the lithospheric plate is anomalously thin and the sub-plate mantle may be anomalously warm in this region (Artemieva, 2019; Lucazeau et al., 1984; Suhadolc et al., 1990; Ziegler, 1992). Additionally, global and regional seismic velocity models display a region of slower than average seismic velocities within the asthenospheric mantle that are consistent with elevated mantle potential temperatures (Figure 14c; Legendre et al., 2012; Schaeffer & Lebedev, 2013).

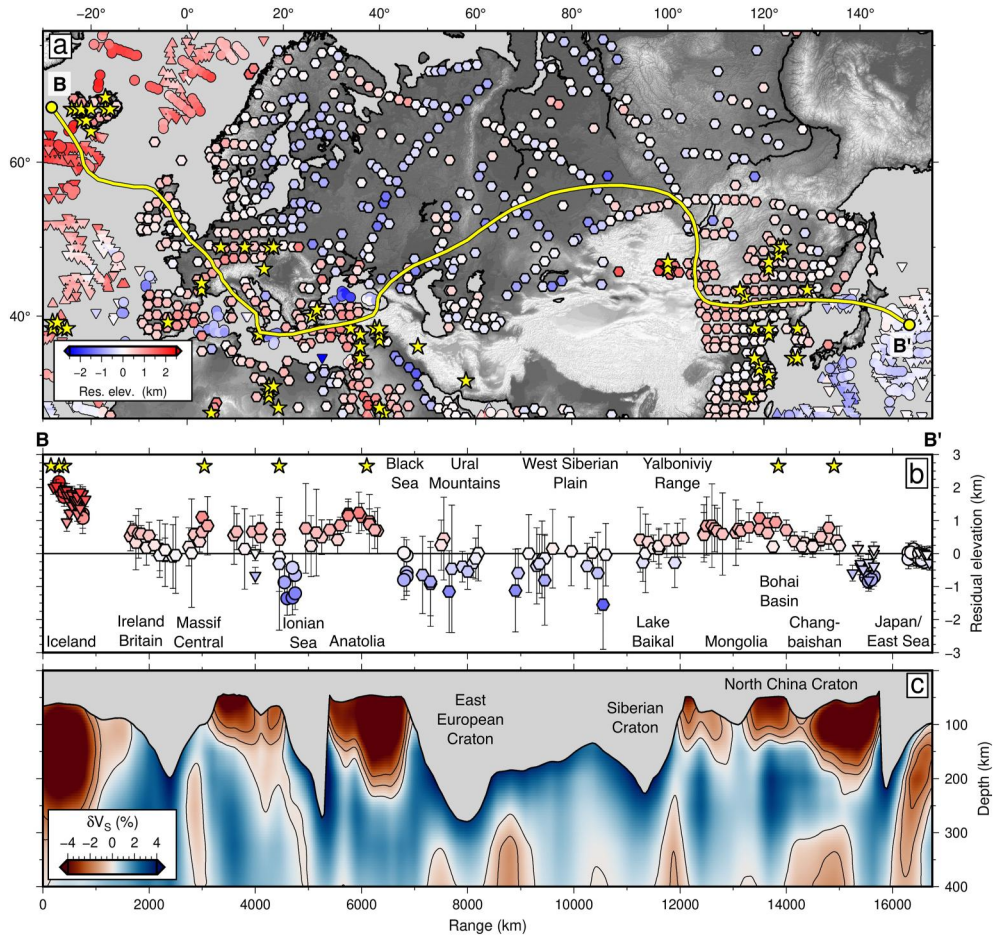

Figure 14. Relationship between residual topography and other data sets in Eurasia. (a) Hexagons = onshore residual topographic estimates (corrected for crustal isostasy), averaged over 4° bins. Circles = most accurate oceanic residual depth estimates; up/down triangles = minimum/maximum oceanic residual depth estimates, where crustal thickness is unconstrained (Hoggard et al., 2017; Holdt et al., 2022). Yellow line = location of transect; yellow stars = location of ≤10 Ma intraplate mafic magmatism Ball et al. (2021). (b) Northwest-to-northeast transect showing residual topography within a 300 km-wide swathe, symbols as before. (c) Vertical slice through SL2013sv shear-wave tomographic model (Schaeffer & Lebedev, 2013). Gray shading = approximate depth to base of lithospheric plate (Hoggard, Czarnota, et al., 2020; Schaeffer & Lebedev, 2013).

Multiple independent lines of evidence indicate that the Anatolian Plateau is sub-crustally supported. A positive residual topographic anomaly of +0.2–1.5 km coincides with the outcrop pattern of Miocene marine limestones that have present-day elevations that exceed ∼1 km. Calibrated inverse modeling of river profiles, exposure dating, and biostratigraphic constraints further suggest that Anatolia was uplifted during Neogene times (McNab et al., 2018; Schildgen et al., 2012). Finally, inverse modeling of both Neogene-to-Recent magmatism and shear-wave velocity anomalies suggests that the lithospheric mantle is anomalously thin and that the asthenosphere is characterized by elevated potential temperatures (Komut et al., 2012; McNab et al., 2018; Şengör et al., 2003).

A 4,000 km-wide negative anomaly with an amplitude of ∼0.0 to ∼−1.5 km straddles the Azov Sea and northern Caucasus in the west, encompasses the Caspian and Aral Seas to Lake Balkhash, and continues to the Tien Shan in the east. Plio-Pleistocene rapid subsidence in the northern Black and Azov Seas has previously been documented in boreholes and on seismic reflection profiles, while a significant subsidence excursion in the south Caspian Sea indicates that in excess of 1 km of anomalous subsidence has occurred in the last 5 Ma (Allen et al., 2002). These anomalies have been previously attributed to crustal shortening or onset of subduction but may also in part be caused by dynamic drawdown (e.g., Brunet et al., 2003). East of the Caspian Sea, information about the vertical motions of the Kazakh Shield is sparse. Nonetheless, this region is underlain by significantly faster than average

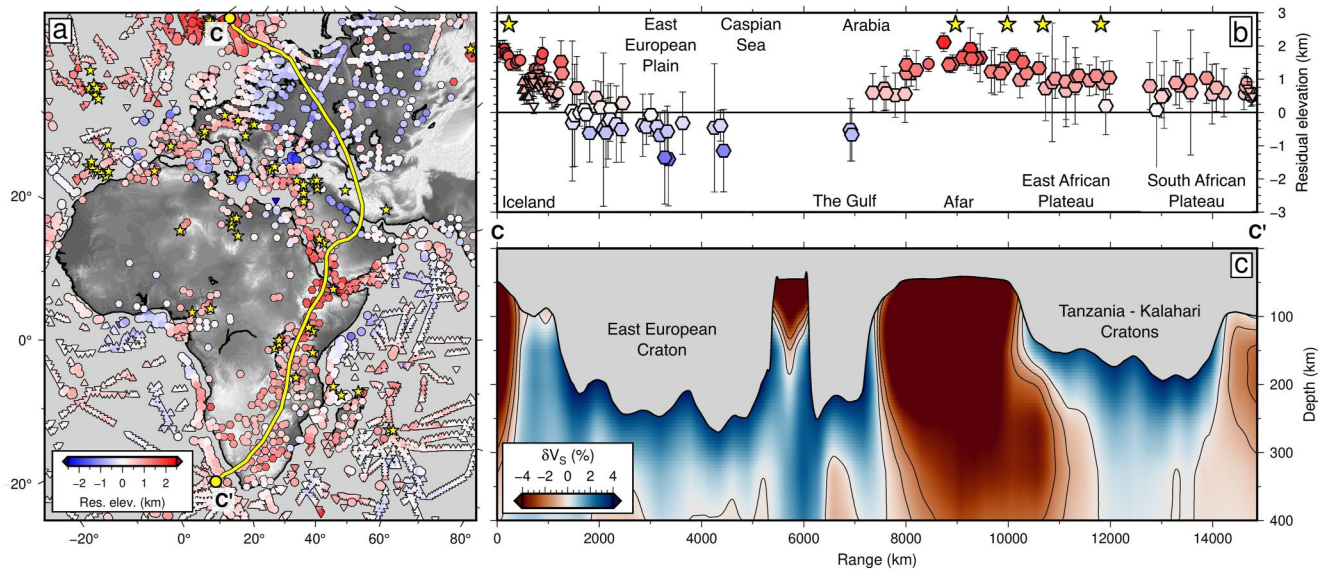

Figure 15. Relationship between residual topography and other data sets in Europe and Africa. (a) Hexagons = onshore residual topographic estimates (after correcting for crustal isostasy), averaged over 4° bins. Circles = most accurate oceanic residual depth estimates; up/down triangles = minimum/maximum oceanic residual depth estimates, where crustal thickness is unconstrained (Hoggard et al., 2017; Holdt et al., 2022). Yellow line = location of transect; yellow stars = location of ≤10 Ma intraplate mafic magmatism Ball et al. (2019, 2021). (b) North-to-south transect showing residual topography within a 300 km-wide swathe, symbols as before. (c) Vertical slice through SL2013sv shear-wave tomographic model (Schaeffer & Lebedev, 2013). Gray shading = approximate depth to base of lithospheric plate (Hoggard, Czarnota, et al., 2020; Schaeffer & Lebedev, 2013).

shear velocities that extend down to >200 km depth, indicating that the region has a thick lithospheric keel (e.g., Hoggard, Czarnota, et al., 2020; Schaeffer & Lebedev, 2013).

Northeast Asia is associated with a 4,000 × 4,000 km swell that extends from Lake Baikal in the north to mainland Southeast Asia in the south, and the Tien Shan in the west to Japan in the east. Note that we exclude a region encompassing the Tibetan Plateau from our analysis owing to complicating factors that relate to active tectonic and orogenic processes. Nevertheless, this region has experienced Neogene-to-Recent volcanism including in the Changbaishan province, which straddles the border between China and North Korea. Neogene magmatism is extensive throughout this region, reaching from northern Korea to the Russian and Mongolian borders in the north, down the Chinese coast to Vietnam and Laos in the south. It has also been proposed that alteration of the North China Craton has resulted in anomalously thin lithospheric mantle in that area (Menzies et al., 2007; R.-X. Zhu et al., 2012). Nonetheless, there is documented evidence for anomalous subsidence within the Bohai Basin during the last 12 Ma, suggesting that any related swell topography must be decreasing in amplitude over this period (Q. Liu et al., 2022).

4.3. Africa

Figure 15 presents a transect from the North Atlantic Ocean to the Cape of Good Hope. An extensive region of anomalously elevated topography occurs in Arabia, eastern and southern Africa, which is in marked contrast to a broad residual topographic depression that characterizes the East European Plain to the north (Figure 15). Residual topographic anomalies are ∼−1 km in the eastern Mediterranean and climb southward and eastward into northern Egypt and the Levant, reaching approximately +2 km in Afar and southern Yemen. A similar tilt is observable from east to west across Arabia from ∼−0.5 to ∼1.0 in the Gulf to ∼+1.5–2.0 km on the Red Sea coast. This extensive swell is spatially coincident with the Oligocene flood basalts of Ethiopia, as well as with ongoing intraplate magmatism. It is known, however, that at least some of the swell topography predates emplacement of basaltic rocks (Sembroni et al., 2016). The Gulf of Aden and Red Sea are both flanked by elevated marine limestones. For example, Paleocene vertebrate fauna including sharks, eagle rays and pycnodont fossils within the Umm Himar Formation crop out at a modern elevation of 1,200 m (Madden et al., 1995). This assemblage is characteristic of estuarine and shallow marine environments. Similar assemblages are found in western Yemen and indicate that pre-rift uplift occurred in early Cenozoic times (Al-Qayim et al., 2005; Al-Subbary et al., 1998). The Red Sea and Gulf

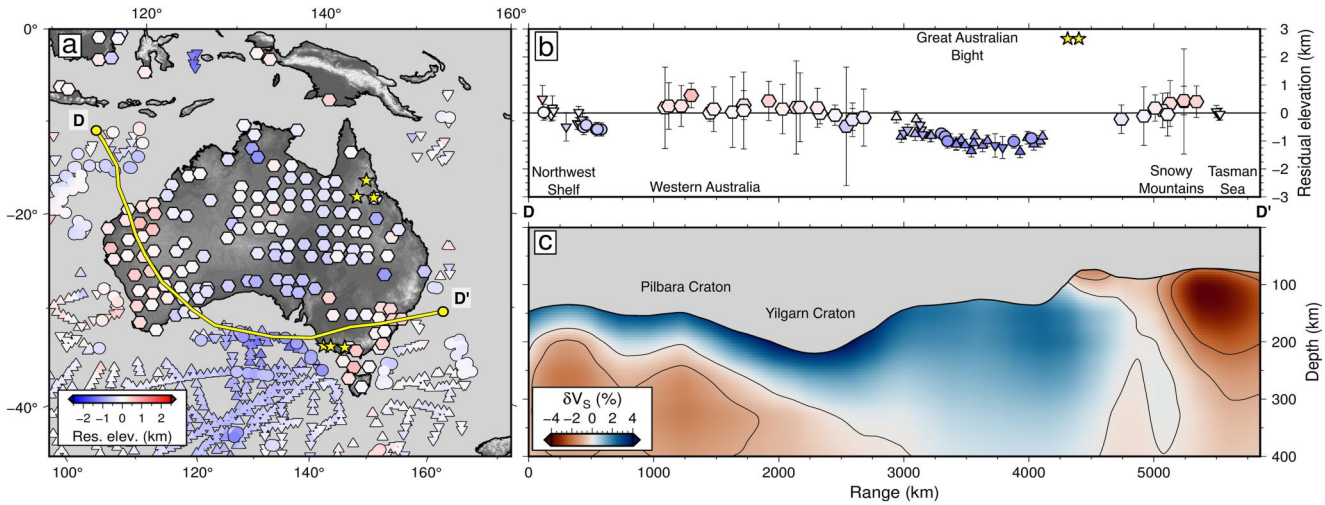

Figure 16. Relationship between residual topography and other data sets in Australia. (a) Hexagons = onshore residual topographic estimates (after correcting for crustal isostasy), averaged over 4° bins. Circles = most accurate oceanic residual depth estimates; up/down triangles = minimum/maximum oceanic residual depth estimates, where crustal thickness is unconstrained (Hoggard et al., 2017; Holdt et al., 2022). Yellow line = location of transect; yellow stars = location of ≤10 Ma intraplate mafic magmatism Ball et al. (2021). (b) Northwest-to-southeast transect showing residual topography within a 300 km-wide swathe, symbols as before. (c) Vertical slice through SL2013sv shear-wave tomographic model (Schaeffer & Lebedev, 2013). Gray shading = approximate depth to base of lithospheric plate (Hoggard, Czarnota, et al., 2020; Schaeffer & Lebedev, 2013).

of Aden are further flanked by extensive Neogene magmatic rocks, inverse modeling of which indicates that asthenospheric potential temperatures are elevated by up to ~100°C (Ball et al., 2021; Wilson et al., 2014). Finally, an extensive, high-amplitude, slow seismic velocity anomaly within the upper mantle indicates that sub-plate temperatures are significantly hotter than ambient values (e.g., Bastow et al., 2008; Boyce et al., 2021). A calibrated conversion between shear-wave velocity and temperature suggests that this temperatures excess could be as large as 200°C (Richards et al., 2020).

Direct evidence for topographic evolution of southern Africa is more sparse. In physiographic terms, it is a low-relief, high-elevation plain that has experienced little erosion since Cretaceous times (Burke & Gunnell, 2008; Guillocheau et al., 2018). It is flanked by rivers that are characterized by significant knickpoints, indicative of a landscape in which uplift is out of equilibrium with erosion. Calibrated inverse modeling of river profiles suggests that this plateau was uplifted during Cenozoic times (O'Malley et al., 2021; Paul et al., 2014). However, an alternative line of argument suggests that it may have been uplifted earlier during Cretaceous times and remained elevated since, while experiencing only minor amounts of erosion (e.g., Wildman et al., 2016). Finally, there is evidence that some combination of these end-members is possible (e.g., Stanley & Flowers, 2023; Stanley et al., 2021). Regardless of the exact timing of topographic uplift, most authors agree that southern African topography is anomalously elevated and that some component of this topography arises from buoyancy within the lower mantle, giving rise to a long-wavelength swell (Gurnis et al., 2000; Lithgow-Bertelloni & Silver, 1998; Nyblade & Robinson, 1994; Richards et al., 2023). This swell is visible in offshore residual depth anomalies, which are in close agreement with our new estimates onshore (Hoggard et al., 2017; Holdt et al., 2022; Robinson et al., 2001). Jones et al. (2017) carried out a multi-observational analysis of the structure of the southern African lithosphere, and also found that topography is anomalously elevated by ~1.4 km. They argued that the origin of anomalous topographic elevation is roughly equally split between reduced density within the lithospheric mantle, owing to melt depletion during cratonisation, and sub-plate support arising from flow within the convecting mantle.

4.4. Australia

A transect extending from the Timor Sea, through the Australian Bight and to the Tasman Sea is shown on Figure 16. On the margins of the Australian continent, there is coherency between onshore residual elevation and offshore oceanic residual depth estimates (Czarnota et al., 2013; Hoggard et al., 2017; Holdt et al., 2022). Western Australia is characterized by elevated residual topography on the order of up to ~500 m. The amplitude of this

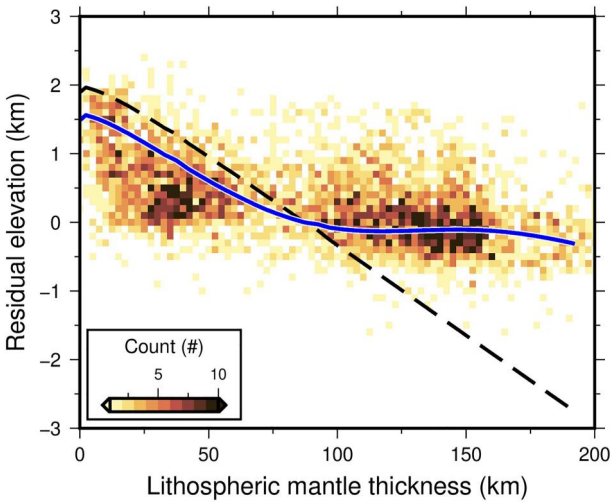

Figure 17. Continental residual topography as a function of lithospheric mantle thickness. Residual topography in 1 × 1° bins as a function of lithospheric mantle thickness (i.e., $z_l - t_{cc}$) from Hoggard, Czarnota, et al. (2020), following correction for crustal thickness, C_t, and density, C_ρ, variations. Black dashed line = isostatic topography due to lithospheric thickness (i.e., C_{lm}) from Equation 24 assuming $t_{cc} = t_{cr} = 32.1$ km and undepleted mantle; blue line = same but for lithospheric mantle that has been chemically depleted according to Equation 25.

anomaly decreases to the south, falling to ∼−200 to −800 m on the northern edge of the Great Australian Bight. Its amplitude is in close agreement with oceanic residual depth estimates, which decrease to around −1 km in the center of a ∼2,000 km-wide depression that is reflected along both the southwestern and southeastern coastlines. This depression is part of the regional expression of the Australia-Antarctic Discordance, which has previously been linked to cold and downwelling mantle (Czarnota et al., 2013; Gurnis et al., 1998; Marks et al., 1990; Ritzwoller et al., 2003). For example, investigations into basalt geochemistry, oceanic crustal thickness and gravity anomalies, indicate that mantle temperatures are below ambient along the mid-oceanic ridge lying above the locus of the depression (Klein et al., 1991; West et al., 1994). The region is also characterized by fast seismic velocities down to a depth of at least 400 km, indicating anomalously cold and presumably dense upper mantle material (Ritzwoller et al., 2003). Eastward this depression, as expressed in both residual topography and bathymetry, shallows and rises onto a ∼+500 m swell that coincides with a region encompassing the Snowy Mountains.

5. Implications for Crustal and Mantle Buoyancy Structure

Our new global database of continental residual topographic anomalies has been constructed by accounting for, and removing the topographic expression of crustal isostasy (i.e., removing topographic variations related to lateral changes in bulk crustal density and thickness). Residual topographic anomalies have peak-to-peak amplitudes of ±1–2 km, vary on wavelengths down to ≤1,000 km, and are likely to be supported by buoyancy variations that have a sub-crustal (i.e., mantle) origin. Here we discuss some of the constraints that our results place upon the structure of the lithosphere and sub-plate mantle.

5.1. Crustal Density Structure

Density of the continental crust generally increases with depth, a component of which is related to the increase in pressure with depth. However, our analysis shows that even after accounting for this factor, there remains an increase in density. In other words, rocks from deep within the crust would have higher density at surface conditions than those that are shallow, indicating that there is a transition toward lithologies with greater density at depth. Furthermore, our analysis has shown that crustal density is higher on average in Precambrian shields and lower in Phanerozoic accreted terranes and sedimentary basins. These insights are consistent with previous work (e.g., Christensen & Mooney, 1995; Laske et al., 2013). Within cratonic regions where $t_{cc} > 30$ km, the density of lower crustal rocks is consistent with granulitic compositions (e.g., Gao et al., 2000; Rudnick & Fountain, 1995). While our density conversion scheme is increasingly unreliable above pressures of 1 GPa, it appears that the rate of density increase reduces at depths greater than ∼45 km.

5.2. Lithospheric Mantle Buoyancy Structure

An important distinction between continental and oceanic estimates of residual topography is that we have not thus far corrected for predicted buoyancy arising from lithospheric thickness variations in the continental realm. Throughout the oceans, the plate cooling relationship results in protracted thickening of the lithospheric plate and concomitant subsidence of the ocean floor. On the continents, a similar phenomenon is well known. Cooling and re-thickening of the lithospheric mantle after rifting leads to subsidence within intracontinental basins and on passive margins (Lachenbruch & Morgan, 1990; D. McKenzie, 1978). Conversely, removal of lithospheric mantle drives surface uplift (e.g., Ball et al., 2021; Bird, 1979; Göğüş & Pysklywec, 2008; Klöcking et al., 2020; Stephenson et al., 2021, 2023). Figure 17 shows the relationship between continental residual topography and estimated present-day thickness of the lithospheric mantle (i.e., $z_l - t_{cc}$) at each measurement site. In this case, the total lithospheric thickness, z_l, has been taken from the model of Hoggard, Czarnota, et al. (2020) and is defined as the depth to the 1,175°C isotherm after converting the shear-wave tomographic model of Schaeffer and Lebedev (2013) to temperature using the approach of Richards et al. (2020). Note that using a different isotherm or

alternative lithospheric thickness model does not materially affect these results (e.g., Priestley et al., 2018). Despite substantial scatter in the relationship, to first order the median value of residual elevation decreases from +0.93 km where $z_l - t_{cc} < 25$ km to −0.11 km where $z_l - t_{cc} > 150$ km. The magnitude of this change is similar to the 0.25 ± 0.56 km total range encompassed by the mean and standard deviation of the entire binned data set (i.e., across all lithospheric and crustal thicknesses). This result confirms that the thickness of the lithospheric mantle places a first-order control on the pattern of sub-crustally supported residual topography (Bird, 1979; Lachenbruch & Morgan, 1990; Lamb et al., 2020; Parsons & Sclater, 1977).

We next attempt to account for this effect by carrying out a correction for isostatic topography supported by the lithospheric mantle. We estimate its density structure by extracting lithospheric thickness, z_l, given by the model of Hoggard, Czarnota, et al. (2020) beneath each crustally corrected and binned residual topographic estimate. We then use this thickness in combination with measured t_{cc} to obtain a steady-state continental geothermal gradient, $T(z)$ that yields $T(z_l) = 1{,}175$°C at the appropriate depth for a mantle potential temperature of $T_p = 1{,}333$°C. This geothermal gradient is generated using the FITPLOT algorithm, which accounts for pressure- and temperature-dependent thermal properties of mantle rocks (Mather et al., 2011). Other FITPLOT parameters are set equivalent to those used in Hoggard, Czarnota, et al. (2020). A key advantage of this approach is that a sub-crustal density profile is constrained in a manner that is consistent with the lithospheric thickness model. The correction for lithospheric isostasy is then given by

$$C_{lm} = \frac{1}{\rho_{m_\circ}}\left[\int_{t_{cr}}^{z_b} \rho_{mr}(z)\,\mathrm{d}z - \int_{t_{cc}-e_r}^{z_b} \rho_m(z)\,\mathrm{d}z\right] \tag{24}$$

where $\rho_{m_\circ}$ is mantle reference density, $\rho_m(z)$ is the local mantle density as a function of depth, $\rho_{mr}(z)$ is the same for the reference column, and $z_b = 350$ km is the depth to the base of the column, at which point $\rho_{mr} \approx \rho_m$.

The black dashed line on Figure 17 shows the magnitude of C_{lm} if we assume that $t_{cc} = t_{cr} = 32.1$ km. Note that varying crustal thickness slightly changes the value of C_{lm}, but does not alter the following discussion. C_{lm} is strongly negative for $z_l - t_{cc} > 100$ km and strongly positive in thinner lithospheric mantle. On the other hand, mean residual topography, which has been corrected for crustal loading alone, is less positive than C_{lm} for small values of $z_l - t_{cc}$, but is significantly less negative for higher values. This discrepancy has important implications for the composition and density structure of the upper mantle, since it points to a progressive decrease in $\rho_{m_\circ}$ at s.t.p. with increasing lithospheric thickness. This density reduction must be caused by compositional rather than thermal or pressure-related effects and indicates the operation of a process that increases buoyancy with respect to a purely thermal lithosphere.

The primary process invoked to explain this behavior is extraction of melts from the lithospheric mantle early in Earth's history such that the residuum is depleted in iron, leading to a decrease in density and an increase in viscosity (e.g., Jordan, 1978; Schutt & Lesher, 2006). Accounting for the topographic expression of this chemical depletion of cratonic roots requires us to parameterize a reduction in bulk lithospheric mantle density as a function of lithospheric thickness (i.e., reduce ρ_m by a factor that is a function of z_l). We use

$$\rho_m^*(z_l) = \rho_m - \frac{1}{2}\mathrm{erf}\left\{\frac{5}{2}\left(\frac{z_l - n}{n}\right) + 1\right\}\Delta\rho_{\max}, \tag{25}$$

where $n = \frac{1}{2}(z_{\min} + z_{\max})$, $\Delta\rho_{\max}$ defines the maximum reduction in density due to depletion, and the parameters $z_{\min}$ and $z_{\max}$ set the lithospheric thickness range over which this density reduction is implemented. Substituting ρ_m^* for ρ_m in Equation 24 yields a correction for lithospheric mantle, C_{lm}^*, that accounts for progressively greater depletion with increasing lithospheric thickness. Setting $\Delta\rho_{\max} = 0.05$ Mg m^{-3}, $z_{\min} = 80$ km and $z_{\max} = 200$ km generates the blue curve in Figure 17.

Treating lithospheric depletion in this manner (i.e., using $\rho_m^*(z_l, \Delta\rho_{\max})$) accounts for the discrepancy between expected and observed residual topography at high values of z_l (blue line in Figure 17). This result indicates that lithospheric depletion is a function of lithospheric thickness, such that depletion is greatest in the thickest lithospheric mantle. It is consistent with an isopycnic condition, which holds that compositional buoyancy increases at approximately the same rate as the increase in density associated with the reduction in average temperature of

thicker lithosphere (Jordan, 1978, 1988; Steinberger, 2016). It also matches theoretical expectations from fluid dynamics that thermal boundary layer thickness is limited by the kinematic viscosity of the mantle, with larger amounts of chemical depletion increasing viscosity of the residuum (Richter & McKenzie, 1981). Furthermore, our results indicate a relatively modest 0.05 Mg m^{-3} (i.e., 1.5%) of maximum depletion, which is well within the bounds of depletion estimates constrained by studies of gravity and the composition of mantle xenoliths (e.g., Crosby et al., 2010; Jordan, 1978; Lee, 2003).

It is also clear from Figure 17 that residual elevation is systematically lower than expected according to the lithospheric correction at thin lithospheric mantle values. This discrepancy could have three causes. First, thin lithospheric mantle is difficult to image using surface wave tomography since crustal velocities can bleed into the mantle. This effect would make thin lithospheric mantle appear absent. Priestley and McKenzie (2013) suggested that any region where $z_l < 100$ km (i.e., $z_l - t_{cc} \approx 70$ km) is likely to be poorly resolved. The approach of Hoggard, Czarnota, et al. (2020) mitigates this bleeding effect but may not completely remove it. The effect of this bias is to push residual topographic estimates that have thin, but present, lithospheric mantle to the left on Figure 17, and thus further below the expected elevation.

Second, in locations where the lithospheric mantle is very thin, then the geothermal gradient in the crust may differ substantially from expected values. This issue arises because thin lithospheric mantle in thermal equilibrium can have an anomalously high geothermal gradient that is not completely accounted for in our parametrization of $T(z)$. This phenomenon will lead to under-correction of seismic velocities for the effects of temperature (i.e., we will under predict the expected seismic velocity at reference conditions). In turn, lower seismic velocities will be manifest as erroneously low crustal density and underpredicted residual topography. In other words, points move downwards on the left-hand side of Figure 17 compared to where they should be positioned. This effect will be even greater in the event that anelastic effects are present at high homologous temperatures (e.g., Yamauchi & Takei, 2016).

Finally, if the value of ρ_{m_o} were to be lower in the lithospheric mantle than the asthenospheric mantle, then removal of a given thickness of lithospheric mantle would lead to lower topography at the surface. Indeed, this effect can be seen on Figure 17. Since we start depleting lithospheric mantle when z_l exceeds 80 km, Equation 25 indicates that the density of the reference lithospheric column of 120 km thickness is already depleted by ~0.4%, resulting in the blue line sitting beneath the black dashed line at thicknesses less than this reference thickness (i.e., at values of $z_l - t_{cc} \leq 87.9$ km on Figure 17). This result may indicate that even average continental lithospheric mantle is depleted to some extent relative to ambient asthenosphere (cf. Wang et al., 2022). Despite these complications, our findings demonstrate that the thickness and compositional buoyancy structure of the lithospheric mantle are important primary and secondary controls, respectively, on continental residual topography.

5.3. Sub-Lithospheric Structure

Our results suggest that, while undoubtedly an important component of residual topography, the contribution of the convecting mantle is difficult to isolate in the continental realm. Nonetheless, we maintain that there are tentative fingerprints of the sub-lithospheric mantle within our residual topographic estimates for five reasons. First, although there are some exceptions, residual topography that is corrected for crustal isostasy alone is often in agreement along continental margins with oceanic residual bathymetric anomalies that have had the plate cooling relationship stripped away (e.g., eastern North America, North Atlantic Ocean, Great Australian Bight, eastern South America, much of Africa). Second, for any given lithospheric thickness bin in Figure 17, the scatter around the central residual topographic value is roughly ±1 km, which is broadly consistent with the scatter in oceanic residual topography after conversion from water- to air-loading (which dampens amplitudes by a factor of ~0.7). Third, variations occur on similar ~1,000 km wavelengths (i.e., spherical harmonic degree $l > 20$) to those in the oceans (Hoggard et al., 2016; Holdt et al., 2022). Fourth, positive residual topography is correlated with both slower than average sub-plate seismic velocities and is coincident with the loci of intraplate magmatism. Taken together, these observations suggest it is likely that some component of swell topography is related to positive temperature anomalies within the asthenosphere. Indeed it has been shown that mantle potential temperatures are negatively correlated with shear-wave velocities at asthenospheric depths (Ball et al., 2021). Finally, almost every constraint on residual topography in Africa is positive, even in locations with thick lithospheric mantle, and Africa also overlies a positive geoid height anomaly. Since the geoid is sensitive to long-wavelength buoyancy structure within the mid and lower mantle, this observation suggests a likely contribution from the deep

mantle (e.g., Gurnis et al., 2000; Jones et al., 2017; Nyblade & Robinson, 1994; Richards et al., 2023). Taken together these lines of evidence indicate some degree of sub-plate topographic support.

This discussion highlights the pitfalls of comparing predictive models of dynamic topography to observational constraints of residual topography in the continental realm. For comparisons to be meaningful, it is vital that models and observations are isolating the same component of the dynamic topographic field (Hoggard et al., 2021; Wang et al., 2022). In particular, this consideration is of great importance if one wishes to isolate only the sub-plate flow component of dynamic topography (Molnar et al., 2015). We contend that this narrow objective is difficult to achieve using continental observations due to substantial isostatic topography generated by the density structure of the lithosphere and asthenospheric mantle. Nonetheless, we have estimated the component of continental topography supported by the full spectrum of mantle processes, which represents an important additional constraint in isolating the sub-plate component.

6. Conclusions

We have collated a comprehensive global inventory of 26,725 local crustal thickness estimates using modern and legacy seismic refraction profiles, deep reflection profiles, and receiver functions. Of these individual estimates, 4,113 provide constraints on crustal velocity structure. We have used these constraints to estimate the component of continental topography that arises as a consequence of crustal thickness and density variations excluding Antarctica and Greenland. In so doing, we have developed a new crustal seismic velocity-to-density conversion scheme by minimizing the misfit between measured and predicted seismic velocities of 1,136 individual laboratory analyses consisting of 149 rock samples across 25 lithologies. By comparison to observed topography, we have been able to estimate continental residual topography, including a careful analysis of its uncertainty, which we have used to investigate spatial patterns of sub-crustal buoyancy structure.

In general, continental residual topographic anomalies have air-loaded amplitudes of ±1.5 km. They are consistent with a range of independent geological and geophysical proxies for sub-crustal topographic support, including long-wavelength free-air gravity anomalies, seismic velocities in the upper mantle, geological markers of surface uplift, and the location of recent intraplate magmatism. Our residual topographic estimates provide a valuable constraint on the present-day planform of sub-crustal buoyancy and can be used to test models of lithospheric density structure and mantle flow. We show that a primary control on the amplitude and spatial distribution of residual topography is the thickness of the lithospheric plate, while important secondary components can be attributed to chemical depletion of cratonic lithosphere and convective flow within the sub-plate mantle.

Data Availability Statement

This study has yielded a number of ancillary tools and datasets. The databases presented in this work are available as follows:

1. SeisCruST, seismic crustal structure and thickness (Database 1 in Supporting Information S1)—a database of crustal thickness measurements, associated seismic velocity profiles and V_P/V_S ratios (Stephenson, Hoggard, Holdt, & Galbraith-Olive, 2024; https://doi.org/10.5281/zenodo.10017428).
2. SMV2rho—software for converting seismic velocities in continental crust (either V_P or V_S) into density as a function of temperature and pressure (Stephenson & Hoggard, 2024; https://doi.org/10.5281/zenodo.10017540).
3. A compilation of laboratory-determined measurements on rock samples of both density at standard temperature and pressure and associated seismic velocities as a function of pressure (Database 2 in Supporting Information S1; also available in the SMV2rho repository).
4. A global database of onshore, air-loaded continental residual topographic estimates (Stephenson, Hoggard, Holdt, & White, 2024; https://doi.org/10.5281/zenodo.10019080).

These data and software are also available in a unified, but static, repository through Geoscience Australia's eCat portal (https://doi.org/10.26186/148960). Note that if users access the data or software through the eCat portal, the appropriate repositories should be cited according to the above information. When using the databases compiled in this study, the following must be cited: (a) this work; (b) the appropriate repository; and (c) the primary work(s)

according to the references listed in the relevant repository's bibliographic database. Full bibliographies for the each data set can be found in its corresponding repository.

Acknowledgments

We thank Karol Czarnota, Marcus Haynes, Fred Richards, Fergus McNab, Victoria Milanez Fernandes, and Karin Sigloch for assistance and discussions. Walter Mooney generously provided a copy of the USGS GSC crustal database of the United States Geological Survey. Hannah Galbraith-Olive helped to compile the crustal database. Shubham Agrawal provided helpful feedback on a draft manuscript. This research was supported by the Australian Government's *Exploring for the Future* program (eCat ID 148960), by an Australian Research Council *Discovery Early Career Researcher Award* (DE220101519), and by the University of Cambridge.

References

Afonso, J. C., Ranalli, G., & Fernàndez, M. (2007). Density structure and buoyancy of the oceanic lithosphere revisited. *Geophysical Research Letters*, *34*(10), L10302. https://doi.org/10.1029/2007gl029515

Airy, G. B. (1855). On the computation of the effect of the attraction of mountain-masses, as disturbing the apparent astronomical latitude of stations in geodetic surveys. *Philosophical Transactions of the Royal Society of London*, *145*, 101–104.

Allen, M. B., Jones, S., Ismail-Zadeh, A., Simmons, M., & Anderson, L. (2002). Onset of subduction as the cause of rapid Pliocene-Quaternary subsidence in the South Caspian basin. *Geology*, *30*(9), 775–778. https://doi.org/10.1130/0091-7613(2002)030<0775:oosatc>2.0.co;2

Al-Qayim, B., Al-Sanabani, J., & Al-Subbary, A. K. (2005). Paleoenvironmental implication of marine bioturbated horizons in the Majzir Formation, western Yemen. *Arabian Journal for Science and Engineering*, *30*, 165–180.

Al-Subbary, A.-K., Nichols, G. J., Bosence, D. W. J., & Al-Kadasi, M. (1998). Pre-rift doming, peneplanation or subsidence in the southern Red Sea? Evidence from the Medj-Zir formation (Tawilah group) of western Yemen. In *Sedimentation and tectonics in rift basins: Red sea—Gulf of Aden* (pp. 119–134). Springer.

Arnould, M., Coltice, N., Flament, N., Seigneur, V., & Müller, R. D. (2018). On the scales of dynamic topography in whole-mantle convection models. *Geochemistry, Geophysics, Geosystems*, *19*(9), 3140–3163. https://doi.org/10.1029/2018gc007516

Artemieva, I. M. (2019). Lithosphere structure in Europe from thermal isostasy. *Earth-Science Reviews*, *188*, 454–468. https://doi.org/10.1016/j.earscirev.2018.11.004

Audet, P. (2014). Toward mapping the effective elastic thickness of planetary lithospheres from a spherical wavelet analysis of gravity and topography. *Physics of the Earth and Planetary Interiors*, *226*, 48–82. https://doi.org/10.1016/j.pepi.2013.09.011

Austermann, J., Mitrovica, J. X., Huybers, P., & Rovere, A. (2017). Detection of a dynamic topography signal in last interglacial sea-level records. *Science Advances*, *3*(7), e1700457. https://doi.org/10.1126/sciadv.1700457

Ball, P., White, N., Maclennan, J., & Stephenson, S. (2021). Global influence of mantle temperature and plate thickness on intraplate volcanism. *Nature Communications*, *12*(1), 2045. https://doi.org/10.1038/s41467-021-22323-9

Ball, P., White, N., Masoud, A., Nixon, S., Hoggard, M., Maclennan, J., et al. (2019). Quantifying asthenospheric and lithospheric controls on mafic magmatism across North Africa. *Geochemistry, Geophysics, Geosystems*, *20*(7), 3520–3555. https://doi.org/10.1029/2019gc008303

Barton, P. (1986). The relationship between seismic velocity and density in the continental crust—A useful constraint? *Geophysical Journal International*, *87*(1), 195–208. https://doi.org/10.1111/j.1365-246x.1986.tb04553.x

Bassin, C. (2000). The current limits of resolution for surface wave tomography in North America. *Eos Transactions American Geophysical Union*, *81*, F897.

Bastow, I., Nyblade, A., Stuart, G., Rooney, T., & Benoit, M. (2008). Upper mantle seismic structure beneath the Ethiopian hot spot: Rifting at the edge of the African low-velocity anomaly. *Geochemistry, Geophysics, Geosystems*, *9*(12), Q12022. https://doi.org/10.1029/2008gc002107

Becker, J. J., Sandwell, D. T., Smith, W. H., Braud, J., Binder, B., Depner, J., et al. (2009). Global bathymetry and elevation data at 30 arc-seconds resolution: SRTM30_PLUS. *Marine Geodesy*, *32*(4), 355–371. https://doi.org/10.1080/01490410903297766

Becker, T. W., Faccenna, C., Humphreys, E. D., Lowry, A. R., & Miller, M. S. (2014). Static and dynamic support of western United States topography. *Earth and Planetary Science Letters*, *402*, 234–246. https://doi.org/10.1016/j.epsl.2013.10.012

Benz, H. M., Unger, J. D., Leith, W. S., Mooney, W. D., Solodilov, L., Egorkin, A. V., & Ryaboy, V. Z. (1992). Deep seismic sounding in northern Eurasia. *Eos, Transactions American Geophysical Union*, *73*(28), 297–300. https://doi.org/10.1029/91eo00233

Bird, P. (1979). Continental delamination and the Colorado plateau. *Journal of Geophysical Research*, *84*(B13), 7561–7571. https://doi.org/10.1029/jb084ib13p07561

Blackwell, D. D., Negraru, P. T., & Richards, M. C. (2006). Assessment of the enhanced geothermal system resource base of the United States. *Natural Resources Research*, *15*(4), 283–308. https://doi.org/10.1007/s11053-007-9028-7

Bouhifd, M. A., Andrault, D., Fiquet, G., & Richet, P. (1996). Thermal expansion of forsterite up to the melting point. *Geophysical Research Letters*, *23*(10), 1143–1146. https://doi.org/10.1029/96gl01118

Boyce, A., Bastow, I., Cottaar, S., Kounoudis, R., Guilloud De Courbeville, J., Caunt, E., & Desai, S. (2021). AFRP20: New P-wavespeed model for the African mantle reveals two whole-mantle plumes below East Africa and Neoproterozoic modification of the Tanzania Craton. *Geochemistry, Geophysics, Geosystems*, *22*(3), e2020GC009302. https://doi.org/10.1029/2020gc009302

Brocher, T. M. (2005). Empirical relations between elastic wavespeeds and density in the Earth's crust. *Bulletin of the Seismological Society of America*, *95*(6), 2081–2092. https://doi.org/10.1785/0120050077

Brunet, M.-F., Korotaev, M. V., Ershov, A. V., & Nikishin, A. M. (2003). The South Caspian basin: A review of its evolution from subsidence modelling. *Sedimentary Geology*, *156*(1–4), 119–148. https://doi.org/10.1016/s0037-0738(02)00285-3

Burke, K., & Gunnell, Y. (2008). *The African erosion surface: A continental-scale synthesis of geomorphology, tectonics, and environmental change over the past 180 million years* (Vol. 201, pp. 1–66). Geological Society of America. https://doi.org/10.1130/2008.1201

Cazenave, A., Dominh, K., Rabinowicz, M., & Ceuleneer, G. (1988). Geoid and depth anomalies over ocean swells and troughs: Evidence of an increasing trend of the geoid-to-depth ratio with age of plate. *Journal of Geophysical Research*, *93*(B7), 8064–8077. https://doi.org/10.1029/jb093ib07p08064

Chambat, F., Ricard, Y., & Valette, B. (2010). Flattening of the Earth: Further from hydrostaticity than previously estimated. *Geophysical Journal International*, *183*(2), 727–732. https://doi.org/10.1111/j.1365-246x.2010.04771.x

Christensen, N. I. (1974). Compressional wave velocities in possible mantle rocks to pressures of 30 kilobars. *Journal of Geophysical Research*, *79*(2), 407–412. https://doi.org/10.1029/jb079i002p00407

Christensen, N. I., & Mooney, W. D. (1995). Seismic velocity structure and composition of the continental crust: A global view. *Journal of Geophysical Research*, *100*(B6), 9761–9788. https://doi.org/10.1029/95jb00259

Christensen, N. I., & Salisbury, M. H. (1975). Structure and constitution of the lower oceanic crust. *Reviews of Geophysics*, *13*(1), 57–86. https://doi.org/10.1029/rg013i001p00057

Cochran, J. R., & Talwani, M. (1977). Free-air gravity anomalies in the world's oceans and their relationship to residual elevation. *Geophysical Journal International*, *50*(3), 495–552. https://doi.org/10.1111/j.1365-246x.1977.tb01334.x

Colli, L., Ghelichkhan, S., & Bunge, H.-P. (2016). On the ratio of dynamic topography and gravity anomalies in a dynamic Earth. *Geophysical Research Letters*, *43*(6), 2510–2516. https://doi.org/10.1002/2016gl067929

Conrad, C. P., & Husson, L. (2009). Influence of dynamic topography on sea level and its rate of change. *Lithosphere*, *1*(2), 110–120. https://doi.org/10.1130/l32.1

Cooper, H., & Simmons, G. (1977). The effect of cracks on the thermal expansion of rocks. *Earth and Planetary Science Letters*, *36*(3), 404–412. https://doi.org/10.1016/0012-821x(77)90065-6

Crosby, A., Fishwick, S., & White, N. (2010). Structure and evolution of the intracratonic Congo Basin. *Geochemistry, Geophysics, Geosystems*, *11*(6), AQ25. https://doi.org/10.1029/2009gc003014

Crosby, A. G., & McKenzie, D. (2009). An analysis of young ocean depth, gravity and global residual topography. *Geophysical Journal International*, *178*(3), 1198–1219. https://doi.org/10.1111/j.1365-246x.2009.04224.x

Cumbaa, S. L., Shimada, K., & Cook, T. D. (2010). Mid-Cenomanian vertebrate faunas of the Western Interior Seaway of North America and their evolutionary, paleobiogeographical, and paleoecological implications. *Palaeogeography, Palaeoclimatology, Palaeoecology*, *295*(1–2), 199–214. https://doi.org/10.1016/j.palaeo.2010.05.038

Czarnota, K., Hoggard, M. J., White, N., & Winterbourne, J. (2013). Spatial and temporal patterns of Cenozoic dynamic topography around Australia. *Geochemistry, Geophysics, Geosystems*, *14*(3), 634–658. https://doi.org/10.1029/2012gc004392

Davies, D. R., Ghelichkhan, S., Hoggard, M., Valentine, A., & Richards, F. D. (2023). Observations and models of dynamic topography: Current status and future directions. In J. C. Duarte (Ed.), *Dynamics of plate tectonics and mantle convection, chap. 11*. Elsevier.

Davies, D. R., Valentine, A. P., Kramer, S. C., Rawlinson, N., Hoggard, M. J., Eakin, C. M., & Wilson, C. R. (2019). Earth's multi-scale topographic response to global mantle flow. *Nature Geoscience*, *12*(10), 845–850. https://doi.org/10.1038/s41561-019-0441-4

Davies, J. H., & Davies, D. R. (2010). Earth's surface heat flux. *Solid Earth*, *1*(1), 5–24. https://doi.org/10.5194/se-1-5-2010

Davis, M. W., White, N. J., Priestley, K. F., Baptie, B. J., & Tilmann, F. J. (2012). Crustal structure of the british isles and its epeirogenic consequences. *Geophysical Journal International*, *190*(2), 705–725. https://doi.org/10.1111/j.1365-246x.2012.05485.x

Ebinger, C., Bechtel, T., Forsyth, D., & Bowin, C. (1989). Effective elastic plate thickness beneath the East African and Afar plateaus and dynamic compensation of the uplifts. *Journal of Geophysical Research*, *94*(B3), 2883–2901. https://doi.org/10.1029/jb094ib03p02883

Faccenna, C., & Becker, T. W. (2020). Topographic expressions of mantle dynamics in the Mediterranean. *Earth-Science Reviews*, *209*, 103327. https://doi.org/10.1016/j.earscirev.2020.103327

Fernandes, V. M., & Roberts, G. G. (2021). Cretaceous-to-Recent net continental uplift from paleobiological data: Insights into sub-plate support. *Bulletin of the Geological Society of America*, *133*(5–6), 1217–1236. https://doi.org/10.1130/b35739.1

Fernandes, V. M., Roberts, G. G., White, N., & Whittaker, A. C. (2019). Continental-scale landscape evolution: A history of North American topography. *Journal of Geophysical Research: Earth Surface*, *124*(11), 2689–2722. https://doi.org/10.1029/2018jf004979

Flament, N., Gurnis, M., & Muller, R. D. (2013). A review of observations and models of dynamic topography. *Lithosphere*, *5*(2), 189–210. https://doi.org/10.1130/l245.1

Forte, A. M., Peltier, W. R., Dziewonski, A. M., & Woodward, R. L. (1993). Dynamic surface topography: A new interpretation based upon mantle flow models derived from seismic tomography. *Geophysical Research Letters*, *20*(3), 225–228. https://doi.org/10.1029/93gl00249

Forte, A. M., & Rowley, D. B. (2022). Earth's isostatic and dynamic topography—A critical perspective. *Geochemistry, Geophysics, Geosystems*, *23*(9), e2021GC009740. https://doi.org/10.1029/2021gc009740

Fountain, D. M. (1976). The Ivrea-Verbano and Strona-Ceneri zones, northern Italy: A cross-section of the continental crust—New evidence from seismic velocities of rock samples. *Tectonophysics*, *33*(1–2), 145–165. https://doi.org/10.1016/0040-1951(76)90054-8

Galloway, W. E., Whiteaker, T. L., & Ganey-Curry, P. (2011). History of Cenozoic North American drainage basin evolution, sediment yield, and accumulation in the Gulf of Mexico Basin. *Geosphere*, *7*(4), 938–973. https://doi.org/10.1130/ges00647.1

Gao, S., Kern, H., Liu, Y.-S., Jin, S.-Y., Popp, T., Jin, Z.-M., et al. (2000). Measured and calculated seismic velocities and densities for granulites from xenolith occurrences and adjacent exposed lower crustal sections: A comparative study from the North China craton. *Journal of Geophysical Research*, *105*(B8), 18965–18976. https://doi.org/10.1029/2000jb900100

Ghelichkhan, S., Bunge, H.-P., & Oeser, J. (2021). Global mantle flow retrodictions for the early Cenozoic using an adjoint method: Evolving dynamic topographies, deep mantle structures, flow trajectories and sublithospheric stresses. *Geophysical Journal International*, *226*(2), 1432–1460. https://doi.org/10.1093/gji/ggab108

Gilligan, A., & Priestley, K. (2018). Lateral variations in the crustal structure of the Indo–Eurasian collision zone. *Geophysical Journal International*, *214*(2), 975–989. https://doi.org/10.1093/gji/ggy172

Glišović, P., & Forte, A. M. (2016). A new back-and-forth iterative method for time-reversed convection modeling: Implications for the Cenozoic evolution of 3-D structure and dynamics of the mantle. *Journal of Geophysical Research: Solid Earth*, *121*(6), 4067–4084. https://doi.org/10.1002/2016jb012841

Göğüş, O. H., & Pysklywec, R. N. (2008). Mantle lithosphere delamination driving plateau uplift and synconvergent extension in eastern Anatolia. *Geology*, *36*(9), 723–726. https://doi.org/10.1130/g24982a.1

Gorbatov, A., Czarnota, K., Henson, P., Fomin, T., Doublier, M., Kennett, B. L. N., & Medlin, A. (2020). Moho variations in northern Australia. In K. Czarnota, I. Roach, S. Abbott, M. Haynes, N. Kositcin, A. Ray, et al. (Eds.), *Exploring for the future: Extended abstracts* (pp. 1–4). Geoscience Australia.

Guerri, M., Cammarano, F., & Connolly, J. A. D. (2015). Effects of chemical composition, water and temperature on physical properties of continental crust. *Geochemistry, Geophysics, Geosystems*, *16*(7), 2431–2449. https://doi.org/10.1002/2015gc005819

Guillocheau, F., Simon, B., Baby, G., Bessin, P., Robin, C., & Dauteuil, O. (2018). Planation surfaces as a record of mantle dynamics: The case example of Africa. *Gondwana Research*, *53*, 82–98. https://doi.org/10.1016/j.gr.2017.05.015

Gurnis, M., Mitrovica, J. X., Ritsema, J., & van Heijst, H.-J. (2000). Constraining mantle density structure using geological evidence of surface uplift rates: The case of the African Superplume. *Geochemistry, Geophysics, Geosystems*, *1*(7), 1020. https://doi.org/10.1029/1999gc000035

Gurnis, M., Müller, R. D., & Moresi, L. (1998). Cretaceous vertical motion of Australia and the Australian-Antarctic Discordance. *Science*, *279*(5356), 1499–1504. https://doi.org/10.1126/science.279.5356.1499

Hager, B. H., Clayton, R. W., Richards, M. A., Comer, R. P., & Dziewonski, A. M. (1985). Lower mantle heterogeneity, dynamic topography and the geoid. *Nature*, *313*(6003), 541–545. https://doi.org/10.1038/313541a0

Hager, B. H., & Richards, M. A. (1989). Long-wavelength variations in Earth's geoid: Physical models and dynamical implications. *Philosophical Transactions of the Royal Society A: Mathematical, Physical & Engineering Sciences*, *328*, 309–327.

Hoggard, M. J., Austermann, J., Randel, C., & Stephenson, S. (2021). *Observational estimates of dynamic topography through space and time, chapter 15* (pp. 371–411). American Geophysical Union.

Hoggard, M. J., Czarnota, K., Richards, F. D., Huston, D. L., Jaques, A. L., & Ghelichkhan, S. (2020). Global distribution of sediment-hosted metals controlled by craton edge stability. *Nature Geoscience*, *13*(7), 504–510. https://doi.org/10.1038/s41561-020-0593-2

Hoggard, M. J., Parnell-Turner, R., & White, N. (2020). Hotspots and mantle plumes revisited: Towards reconciling the mantle heat transfer discrepancy. *Earth and Planetary Science Letters*, *542*, 116317. https://doi.org/10.1016/j.epsl.2020.116317

Hoggard, M. J., White, N., & Al-Attar, D. (2016). Global dynamic topography observations reveal limited influence of large-scale mantle flow. *Nature Geoscience*, *9*(6), 456–463. https://doi.org/10.1038/ngeo2709

Hoggard, M. J., Winterbourne, J., Czarnota, K., & White, N. (2017). Oceanic residual depth measurements, the plate cooling model, and global dynamic topography. *Journal of Geophysical Research: Solid Earth*, *122*(3), 2328–2373. https://doi.org/10.1002/2016jb013457

Holdt, M. C., White, N. J., Stephenson, S. N., & Conway-Jones, B. W. (2022). Densely sampled global dynamic topographic observations and their significance. *Journal of Geophysical Research: Solid Earth*, *127*(7), e2022JB024391. https://doi.org/10.1029/2022jb024391

Holford, S. P., Green, P. F., Hillis, R. R., Underhill, J. R., Stoker, M. S., & Duddy, I. R. (2010). Multiple post-Caledonian exhumation episodes across NW Scotland revealed by apatite fission-track analysis. *Journal of the Geological Society*, *167*(4), 675–694. https://doi.org/10.1144/0016-76492009-167

Hopper, E., & Fischer, K. M. (2018). The changing face of the lithosphere-asthenosphere boundary: Imaging continental scale patterns in upper mantle structure across the contiguous U.S. with Sp converted waves. *Geochemistry, Geophysics, Geosystems*, *19*(8), 2593–2614. https://doi.org/10.1029/2018gc007476

Houtgast, R., & Van Balen, R. (2000). Neotectonics of the Roer Valley Rift system, The Netherlands. *Global and Planetary Change*, *27*(1–4), 131–146. https://doi.org/10.1016/s0921-8181(01)00063-7

Ji, S., Li, A., Wang, Q., Long, C., Wang, H., Marcotte, D., & Salisbury, M. (2013). Seismic velocities, anisotropy, and shear-wave splitting of antigorite serpentinites and tectonic implications for subduction zones. *Journal of Geophysical Research: Solid Earth*, *118*(3), 1015–1037. https://doi.org/10.1002/jgrb.50110

Ji, S., Sun, S., Wang, Q., & Marcotte, D. (2010). Lamé parameters of common rocks in the Earth's crust and upper mantle. *Journal of Geophysical Research*, *115*(B6), B063141. https://doi.org/10.1029/2009jb007134

Ji, S., Wang, Q., & Salisbury, M. H. (2009). Composition and tectonic evolution of the Chinese continental crust constrained by Poisson's ratio. *Tectonophysics*, *463*(1–4), 15–30. https://doi.org/10.1016/j.tecto.2008.09.007

Ji, S., Wang, Q., Salisbury, M. H., Wang, Y., & Jia, D. (2016). P-wave velocities and anisotropy of typical rocks from the Yunkai Mts.(Guangdong and Guangxi, China) and constraints on the composition of the crust beneath the South China Sea. *Journal of Asian Earth Sciences*, *131*, 40–61. https://doi.org/10.1016/j.jseaes.2016.09.006

Johnson, S. E., Song, W. J., Cook, A. C., Vel, S. S., & Gerbi, C. C. (2021). The quartz $\alpha \leftrightarrow \beta$ phase transition: Does it drive damage and reaction in continental crust? *Earth and Planetary Science Letters*, *553*, 116622. https://doi.org/10.1016/j.epsl.2020.116622

Jones, A. G., Afonso, J. C., & Fullea, J. (2017). Geochemical and geophysical constrains on the dynamic topography of the Southern African Plateau. *Geochemistry, Geophysics, Geosystems*, *18*(10), 3556–3575. https://doi.org/10.1002/2017gc006908

Jordan, T. H. (1978). Composition and development of the continental tectosphere. *Nature*, *274*(5671), 544–548. https://doi.org/10.1038/274544a0

Jordan, T. H. (1988). Structure and formation of the continental tectosphere. *Journal of Petrology, Special Lithosphere Issue*, *1*, 11–37. https://doi.org/10.1093/petrology/special_volume.1.11

Julià, J., Jagadeesh, S., Rai, S. S., & Owens, T. J. (2009). Deep crustal structure of the Indian shield from joint inversion of P wave receiver functions and Rayleigh wave group velocities: Implications for Precambrian crustal evolution. *Journal of Geophysical Research*, *114*(B10), B10313. https://doi.org/10.1029/2008jb006261

Karlstrom, K. E., Crow, R., Crossey, L. J., Coblentz, D., & Van Wijk, J. (2008). Model for tectonically driven incision of the younger than 6 Ma Grand Canyon. *Geology*, *36*(11), 835–838. https://doi.org/10.1130/g25032a.1

Kaufmann, E. (1977). Upper Cretaceous cyclothems, biotas and environments. *Rock Canyon anticline, Pueblo, Colorado: The Mountain Geologist*, *14*, 129–152.

Kennett, B. L., Gorbatov, A., Yuan, H., Agrawal, S., Murdie, R., Doublier, M., et al. (2023). Refining the Moho across the Australian continent. *Geophysical Journal International*, *233*(3), 1863–1877. https://doi.org/10.1093/gji/ggad035

Kern, H., & Richter, A. (1981). Temperature derivatives of compressional and shear wave velocities in crustal and mantle rocks at 6 kbar confining pressure. *Journal of Geophysics*, *49*, 47–56.

Klein, E. M., Langmuir, C. H., & Staudigel, H. (1991). Geochemistry of basalts from the southeast Indian ridge, 115°E–138°E. *Journal of Geophysical Research*, *96*(B2), 2089–2107. https://doi.org/10.1029/90jb01384

Klöcking, M., Hoggard, M. J., Rodríguez Tribaldos, V., Richards, F. D., Guimarães, A. R., Maclennan, J., & White, N. J. (2020). A tale of two domes: Neogene to recent volcanism and dynamic uplift of northeast Brazil and southwest Africa. *Earth and Planetary Science Letters*, *547*, 116464. https://doi.org/10.1016/j.epsl.2020.116464

Klöcking, M., White, N. J., Maclennan, J., McKenzie, D., & Fitton, J. G. (2018). Quantitative relationships between basalt geochemistry, shear wave velocity, and asthenospheric temperature beneath western North America. *Geochemistry, Geophysics, Geosystems*, *19*(9), 3376–3404. https://doi.org/10.1029/2018gc007559

Komut, T., Gray, R., Pysklywec, R., & Göğüş, O. H. (2012). Mantle flow uplift of western Anatolia and the Aegean: Interpretations from geophysical analyses and geodynamic modeling. *Journal of Geophysical Research*, *117*(B11), 412. https://doi.org/10.1029/2012jb009306

Lachenbruch, A. H., & Morgan, P. (1990). Continental extension, magmatism and elevation: Formal relations and rules of thumb. *Tectonophysics*, *174*(1–2), 39–62. https://doi.org/10.1016/0040-1951(90)90383-j

Lamb, S., Moore, J. D., Perez-Gussinye, M., & Stern, T. (2020). Global whole-lithosphere isostasy: Implications for surface elevations, structure, strength, and densities of the continental lithosphere. *Geochemistry, Geophysics, Geosystems*, *21*(10), e2020GC009150. https://doi.org/10.1029/2020gc009150

Laske, G., Masters, G., Ma, Z., & Pasyanos, M. (2013). Update on CRUST1.0—A 1-degree global model of Earth's crust. In *EGU general assembly abstracts*.

Lee, C.-T. A. (2003). Compositional variation of density and seismic velocities in natural peridotites at STP conditions: Implications for seismic imaging of compositional heterogeneities in the upper mantle. *Journal of Geophysical Research*, *108*(B92), 441. https://doi.org/10.1029/2003jb002413

Legendre, C., Meier, T., Lebedev, S., Friederich, W., & Viereck-Götte, L. (2012). A shear wave velocity model of the European upper mantle from automated inversion of seismic shear and surface waveforms. *Geophysical Journal International*, *191*(1), 282–304. https://doi.org/10.1111/j.1365-246x.2012.05613.x

Levander, A., Schmandt, B., Miller, M., Liu, K., Karlstrom, K., Crow, R., et al. (2011). Continuing Colorado Plateau uplift by delamination-style convective lithospheric downwelling. *Nature*, *472*(7344), 461–465. https://doi.org/10.1038/nature10001

Levandowski, W., Jones, C. H., Shen, W., Ritzwoller, M. H., & Schulte-Pelkum, V. (2014). Origins of topography in the western US: Mapping crustal and upper mantle density variations using a uniform seismic velocity model. *Journal of Geophysical Research: Solid Earth*, *119*(3), 2375–2396. https://doi.org/10.1002/2013jb010607

Lithgow-Bertelloni, C., & Silver, P. G. (1998). Dynamic topography, plate driving forces and the African superswell. *Nature*, *395*(6699), 269–272. https://doi.org/10.1038/26212

Liu, L., & Gurnis, M. (2010). Dynamic subsidence and uplift of the Colorado Plateau. *Geology*, *38*(7), 663–666. https://doi.org/10.1130/g30624.1

Liu, Q., He, L., Yi, Z., & Zhang, L. (2022). Anomalous post-rift subsidence in the Bohai Bay Basin, Eastern China: Contributions from mantle process and fault activity. *Tectonics*, *41*(1), e2021TC006748. https://doi.org/10.1029/2021tc006748

Lucazeau, F., Vasseur, G., & Bayer, R. (1984). Interpretation of heat flow data in the French Massif Central. *Tectonophysics*, *103*(1–4), 99–119. https://doi.org/10.1016/0040-1951(84)90077-5

Ludwig, W. J., Nafe, J. E., & Drake, C. L. (1970). Seismic refraction. In A. E. Maxwell (Ed.) *The sea* (Vol. 4, pp. 53–84). Wiley-Interscience.

Ma, X., & Lowry, A. R. (2017). USArray imaging of continental crust in the conterminous United States. *Tectonics*, *36*(12), 2882–2902. https://doi.org/10.1002/2017tc004540

Mackay, L. M., & White, N. J. (2006). Accurate estimates of the spatial pattern of denudation by inversion of stacking velocity data: An example from the British Isles. *Geochemistry, Geophysics, Geosystems*, *7*(10), Q06010. https://doi.org/10.1029/2005gc001192

Madden, C. T., Whitmore, F. C. J., Schmidt, D. L., & Mohammed Naqvi, I. (1995). The Umm Himar Formation (Paleocene) of Saudi Arabia and associated strata: Stratigraphy, vertebrate fauna, and paleoenvironment. In F. C. Whitmore & C. T. Madden (Eds.), *Paleocene vertebrates from Jabal Umm Himar, Kingdom of Saudi Arabia, chapter A* (pp. A1–A19). US Government Printing Office.

Marks, K. M., & Sandwell, D. T. (1991). Analysis of geoid height versus topography for oceanic plateaus and swells using nonbiased linear regression. *Journal of Geophysical Research*, *96*(B5), 8045–8055. https://doi.org/10.1029/91jb00240

Marks, K. M., Vogt, P. R., & Hall, S. A. (1990). Residual depth anomalies and the origin of the Australian-Antarctic Discordance Zone. *Journal of Geophysical Research*, *95*(B11), 17325–17337. https://doi.org/10.1029/jb095ib11p17325

Mather, K. A., Pearson, D. G., McKenzie, D., Kjarsgaard, B. A., & Priestley, K. (2011). Constraints on the depth and thermal history of cratonic lithosphere from peridotite xenoliths, xenocrysts and seismology. *Lithos*, *125*(1–2), 729–742. https://doi.org/10.1016/j.lithos.2011.04.003

Matthews, S., Shorttle, O., & Maclennan, J. (2016). The temperature of the Icelandic mantle from olivine-spinel aluminum exchange thermometry. *Geochemistry, Geophysics, Geosystems*, *17*(11), 4725–4752. https://doi.org/10.1002/2016gc006497

McKenzie, D. (1978). Some remarks on the development of sedimentary basins. *Earth and Planetary Science Letters*, *40*(1), 25–32. https://doi.org/10.1016/0012-821x(78)90071-7

McKenzie, D., & Fairhead, D. (1997). Estimates of the effective elastic thickness of the continental lithosphere from Bouguer and free-air gravity anomalies. *Journal of Geophysical Research*, *102*(B12), 27523–27552. https://doi.org/10.1029/97jb02481

McKenzie, D., Jackson, J., & Priestley, K. (2005). Thermal structure of oceanic and continental lithosphere. *Earth and Planetary Science Letters*, *233*(3–4), 337–349. https://doi.org/10.1016/j.epsl.2005.02.005

McKenzie, D. P., Roberts, J. M., & Weiss, N. O. (1974). Convection in the Earth's mantle: Towards a numerical simulation. *Journal of Fluid Mechanics*, *62*(03), 465–538. https://doi.org/10.1017/s0022112074000784

McNab, F., Ball, P. W., Hoggard, M. J., & White, N. J. (2018). Neogene uplift and magmatism of Anatolia: Insights from drainage analysis and basaltic geochemistry. *Geochemistry, Geophysics, Geosystems*, *19*(1), 175–213. https://doi.org/10.1002/2017gc007251

Menard, H. W. (1965). Sea-floor relief and mantle convection. *Physics and Chemistry of the Earth*, *6*, 315–364. https://doi.org/10.1016/0079-1946(65)90017-0

Menzies, M., Xu, Y., Zhang, H., & Fan, W. (2007). Integration of geology, geophysics and geochemistry: A key to understanding the North China craton. *Lithos*, *96*(1–2), 1–21. https://doi.org/10.1016/j.lithos.2006.09.008

Molnar, P., England, P. C., & Jones, C. H. (2015). Mantle dynamics, isostasy, and the support of high terrain. *Journal of Geophysical Research: Solid Earth*, *120*(3), 1932–1957. https://doi.org/10.1002/2014jb011724

Mooney, W. D. (2015). Crust and lithospheric structure—Global crustal structure. In G. Schubert (Ed.), *Treatise on geophysics, chapter 11* (2nd ed., pp. 339–390). Elsevier.

Mooney, W. D., Barrera-Lopez, C., Suárez, M. G., & Castelblanco, M. A. (2023). Earth crustal model 1 (ecm1): A 1° × 1° global seismic and density model. *Earth-Science Reviews*, *243*, 104493. https://doi.org/10.1016/j.earscirev.2023.104493

Mooney, W. D., Laske, G., & Masters, T. G. (1998). Crust 5.1: A global crustal model at 5° × 5°. *Journal of Geophysical Research*, *103*(B1), 727–747. https://doi.org/10.1029/97jb02122

Moucha, R., Forte, A. M., Mitrovica, J. X., Rowley, D. B., Quéré, S., Simmons, N. A., & Grand, S. P. (2008). Dynamic topography and long-term sea-level variations: There is no such thing as a stable continental platform. *Earth and Planetary Science Letters*, *271*(1–4), 101–108. https://doi.org/10.1016/j.epsl.2008.03.056

Moucha, R., Forte, A. M., Rowley, D. B., Mitrovica, J. X., Simmons, N. A., & Grand, S. P. (2009). Deep mantle forces and the uplift of the Colorado Plateau. *Geophysical Research Letters*, *36*(19), L19310. https://doi.org/10.1029/2009gl039778

Nyblade, A. A., & Robinson, S. W. (1994). The African superswell. *Geophysical Research Letters*, *21*(9), 765–768. https://doi.org/10.1029/94gl00631

Ohno, I. (1995). Temperature variation of elastic properties of α-quartz up to the α–β transition. *Journal of Physics of the Earth*, *43*(2), 157–169. https://doi.org/10.4294/jpe1952.43.157

O'Malley, C. P. B., White, N. J., Roberts, G. G., & Stephenson, S. N. (2021). Large-scale tectonic forcing of the African landscape and its drainage patterns. *Geochemistry, Geophysics, Geosystems*, *126*(12), e2021JF006345. https://doi.org/10.1029/2021jf006345

Pari, G., & Peltier, W. R. (2000). Subcontinental mantle dynamics: A further analysis based on the joint constraints of dynamic surface topography and free-air gravity. *Journal of Geophysical Research*, *105*(B3), 5635–5662. https://doi.org/10.1029/1999jb900349

Parsons, B., & Daly, S. (1983). The relationship between surface topography, gravity anomalies, and temperature structure of convection. *Journal of Geophysical Research*, *88*(B2), 1129–1144. https://doi.org/10.1029/jb088ib02p01129

Parsons, B., & Sclater, J. G. (1977). An analysis of the variation of ocean floor bathymetry and heat flow with age. *Journal of Geophysical Research*, *82*(5), 803–827. https://doi.org/10.1029/jb082i005p00803

Paul, J. D., Roberts, G. G., & White, N. (2014). The African landscape through space and time. *Tectonics*, *33*(6), 898–935. https://doi.org/10.1002/2013tc003479

Pekeris, C. L. (1935). Thermal convection in the interior of the Earth. *Geophysical Journal International*, *3*, 343–367. https://doi.org/10.1111/j.1365-246x.1935.tb01742.x

Peltier, W. R. (1994). Ice age paleotopography. *Science*, *265*(5169), 195–201. https://doi.org/10.1126/science.265.5169.195

Plank, T., & Forsyth, D. W. (2016). Thermal structure and melting conditions in the mantle beneath the Basin and Range province from seismology and petrology. *Geochemistry, Geophysics, Geosystems*, *17*(4), 2825–2834. https://doi.org/10.1002/2015gc006205

Pratt, J. H. (1855). On the attraction of the Himalaya Mountains, and of the elevated regions beyond them, upon the plumb-line in India. *Philosophical Transactions of the Royal Society of London*, *145*, 53–100.

Priestley, K., & McKenzie, D. (2006). The thermal structure of the lithosphere from shear-wave velocities. *Earth and Planetary Science Letters*, *244*(1–2), 285–301. https://doi.org/10.1016/j.epsl.2006.01.008
Priestley, K., & McKenzie, D. (2013). The relationship between shear-wave velocity, temperature, attenuation and viscosity in the shallow part of the mantle. *Earth and Planetary Science Letters*, *381*, 78–91. https://doi.org/10.1016/j.epsl.2013.08.022
Priestley, K., McKenzie, D., & Ho, T. (2018). A lithosphere-asthenosphere boundary—A global model derived from multimode surface-wave tomography and petrology. In B. Romanowicz & H. Yuan (Eds.), *Geophysical monograph series: Lithospheric discontinuities* (Vol. 239, pp. 111–124). American Geophysical Union.
Ricard, Y., Richards, M., Lithgow-Bertelloni, C., & Le Stunff, Y. (1993). A geodynamic model of mantle density heterogeneity. *Journal of Geophysical Research*, *98*(B12), 21895–21909. https://doi.org/10.1029/93jb02216
Richards, F. D., Hoggard, M. J., Cowton, L. R., & White, N. J. (2018). Reassessing the thermal structure of oceanic lithosphere with revised global inventories of basement depths and heat flow measurements. *Journal of Geophysical Research: Solid Earth*, *123*(10), 9136–9161. https://doi.org/10.1029/2018jb015998
Richards, F. D., Hoggard, M. J., Ghelichkhan, S., Koelemeijer, P., & Lau, H. C. P. (2023). Geodynamic, geodetic, and seismic constraints favour deflated and dense-cored LLVPs. *Earth and Planetary Science Letters*, *602*, 117964. https://doi.org/10.1016/j.epsl.2022.117964
Richards, F. D., Hoggard, M. J., White, N., & Ghelichkhan, S. (2020). Quantifying the relationship between short-wavelength dynamic topography and thermomechanical structure of the upper mantle using calibrated parameterization of anelasticity. *Journal of Geophysical Research: Solid Earth*, *125*(9), e2019JB019062. https://doi.org/10.1029/2019jb019062
Richter, F. M., & McKenzie, D. P. (1981). Parameterizations for the horizontally averaged temperature of infinite Prandtl number convection. *Journal of Geophysical Research*, *86*(B3), 1738–1744. https://doi.org/10.1029/jb086ib03p01738
Rickers, F., Fichtner, A., & Trampert, J. (2013). The Iceland–Jan Mayen plume system and its impact on mantle dynamics in the North Atlantic region: Evidence from full-waveform inversion. *Earth and Planetary Science Letters*, *367*, 39–51. https://doi.org/10.1016/j.epsl.2013.02.022
Ritzwoller, M. H., Shapiro, N. M., & Leahy, G. M. (2003). A resolved mantle anomaly as the cause of the Australian-Antarctic Discordance. *Journal of Geophysical Research*, *108*(B12), 2559. https://doi.org/10.1029/2003jb002522
Roberts, G. G., White, N. J., Martin-Brandis, G. L., & Crosby, A. G. (2012). An uplift history of the Colorado Plateau and its surroundings from inverse modeling of longitudinal river profiles. *Tectonics*, *31*(4), TC4022. https://doi.org/10.1029/2012tc003107
Robinson, C. J., Bickle, M. J., Minshull, T. A., White, R. S., & Nichols, A. R. L. (2001). Low degree melting under the Southwest Indian Ridge: The roles of mantle temperature, conductive cooling and wet melting. *Earth and Planetary Science Letters*, *188*(3–4), 383–398. https://doi.org/10.1016/s0012-821x(01)00329-6
Rudnick, R. L., & Fountain, D. M. (1995). Nature and composition of the continental crust: A lower crustal perspective. *Reviews of Geophysics*, *33*(3), 267–309. https://doi.org/10.1029/95rg01302
Sahagian, D. (1987). Epeirogeny and eustatic sea level changes as inferred from Cretaceous shoreline deposits: Applications to the central and western United States. *Journal of Geophysical Research*, *92*(B6), 4895–4904. https://doi.org/10.1029/jb092ib06p04895
Schaeffer, A. J., & Lebedev, S. (2013). Global shear speed structure of the upper mantle and transition zone. *Geophysical Journal International*, *194*(1), 417–449. https://doi.org/10.1093/gji/ggt095
Schaeffer, A. J., & Lebedev, S. (2014). Imaging the North American continent using waveform inversion of global and USArray data. *Earth and Planetary Science Letters*, *402*, 26–41. https://doi.org/10.1016/j.epsl.2014.05.014
Schildgen, T. F., Cosentino, D., Bookhagen, B., Niedermann, S., Yıldırım, C., Echtler, H., et al. (2012). Multi-phased uplift of the southern margin of the central Anatolian Plateau, Turkey: A record of tectonic and upper mantle processes. *Earth and Planetary Science Letters*, *317*, 85–95. https://doi.org/10.1016/j.epsl.2011.12.003
Schilling, J.-G. (1973). Iceland mantle plume: Geochemical study of Reykjanes Ridge. *Nature*, *242*(5400), 565–571. https://doi.org/10.1038/242565a0
Schoonman, C., White, N., & Pritchard, D. (2017). Radial viscous fingering of hot asthenosphere within the Icelandic plume beneath the North Atlantic Ocean. *Earth and Planetary Science Letters*, *468*, 51–61. https://doi.org/10.1016/j.epsl.2017.03.036
Schrank, C., Fusseis, F., Karrech, A., & Regenauer-Lieb, K. (2012). Thermal-elastic stresses and the criticality of the continental crust. *Geochemistry, Geophysics, Geosystems*, *13*(9), 1–21. https://doi.org/10.1029/2012gc004085
Schutt, D., & Lesher, C. (2006). Effects of melt depletion on the density and seismic velocity of garnet and spinel lherzolite. *Journal of Geophysical Research*, *111*(B5), B05401. https://doi.org/10.1029/2003jb002950
Sembroni, A., Faccenna, C., Becker, T. W., Molin, P., & Abebe, B. (2016). Long-term, deep-mantle support of the Ethiopia-Yemen Plateau. *Tectonics*, *35*(2), 469–488. https://doi.org/10.1002/2015tc004000
Şengör, A., Özeren, S., Genç, T., & Zor, E. (2003). East Anatolian high plateau as a mantle-supported, north-south shortened domal structure. *Geophysical Research Letters*, *30*(24), 248045. https://doi.org/10.1029/2003gl017858
Sigloch, K. (2011). Mantle provinces under North America from multifrequency P-wave tomography. *Geochemistry, Geophysics, Geosystems*, *12*(2), Q02W08. https://doi.org/10.1029/2010gc003421
Soares, J. E., Berrocal, J., Fuck, R. A., Mooney, W. D., & Ventura, D. B. (2006). Seismic characteristics of central Brazil crust and upper mantle: A deep seismic refraction study. *Journal of Geophysical Research*, *111*(B12), B12302. https://doi.org/10.1029/2005jb003769
Spasojevic, S., & Gurnis, M. (2012). Sea level and vertical motion of continents from dynamic earth models since the late cretaceous. *AAPG Bulletin*, *96*(11), 2037–2064. https://doi.org/10.1306/03261211121
Stanley, J. R., Braun, J., Baby, G., Guillocheau, F., Robin, C., Flowers, R. M., et al. (2021). Constraining plateau uplift in southern Africa by combining thermochronology, sediment flux, topography, and landscape evolution modeling. *Journal of Geophysical Research: Solid Earth*, *126*(7), e2020JB021243. https://doi.org/10.1029/2020jb021243
Stanley, J. R., & Flowers, R. M. (2023). Localized cenozoic erosion on the southern African plateau: A signal of topographic uplift? *Geology*, *51*(6), 549–553. https://doi.org/10.1130/g50790.1
Stein, C. A., & Stein, S. (1992). A model for the global variation in oceanic depth and heat flow with lithospheric age. *Nature*, *355*, 472–475.
Steinberger, B. (2016). Topography caused by mantle density variations: Observation-based estimates and models derived from tomography and lithosphere thickness. *Geophysical Journal International*, *205*(1), 604–621. https://doi.org/10.1093/gji/ggw040
Steinberger, B., Conrad, C. P., Tutu, A. O., & Hoggard, M. J. (2019). On the amplitude of dynamic topography at spherical harmonic degree two. *Tectonophysics*, *760*, 221–228. https://doi.org/10.1016/j.tecto.2017.11.032
Stephenson, S. N., Ball, P. W., & Richards, F. D. (2023). Destruction and regrowth of lithospheric mantle beneath large igneous provinces. *Science Advances*, *9*(36), eadf6216. https://doi.org/10.1126/sciadv.adf6216
Stephenson, S. N., & Hoggard, M. J. (2024). SMV2rho: Crustal density from seismic velocity [Software]. *Zenodo*. https://doi.org/10.5281/zenodo.10017540

Stephenson, S. N., Hoggard, M. J., Holdt, M. C., & Galbraith-Olive, H. (2024). SeisCruST: Seismic crustal structure and thickness [Dataset]. *Zenodo*. https://doi.org/10.5281/zenodo.10017428

Stephenson, S. N., Hoggard, M. J., Holdt, M. C., & White, N. (2024). Global residual topography [Dataset]. *Zenodo*. https://doi.org/10.5281/zenodo.10019080

Stephenson, S. N., Roberts, G. G., Hoggard, M. J., & Whittaker, A. C. (2014). A Cenozoic uplift history of Mexico and its surroundings from longitudinal river profiles. *Geochemistry, Geophysics, Geosystems*, *15*(12), 4734–4758. https://doi.org/10.1002/2014gc005425

Stephenson, S. N., White, N., Carter, A., Seward, D., Ball, P., & Klöcking, M. (2021). Cenozoic dynamic topography of Madagascar. *Geochemistry, Geophysics, Geosystems*, *22*(6), e2020GC009624. https://doi.org/10.1029/2020gc009624

Stierman, D. J., Healy, J. H., & Kovach, R. L. (1979). Pressure-induced velocity gradient: An alternative to a Pg refractor in the Gabilan Range, central California. *Bulletin of the Seismological Society of America*, *69*, 397–415.

Suhadolc, P., Panza, G. F., & Mueller, S. (1990). Physical properties of the lithosphere—Asthenosphere system in Europe. *Tectonophysics*, *176*(1–2), 123–135. https://doi.org/10.1016/0040-1951(90)90262-7

Szwillus, W., Afonso, J. C., Ebbing, J., & Mooney, W. D. (2019). Global crustal thickness and velocity structure from geostatistical analysis of seismic data. *Journal of Geophysical Research: Solid Earth*, *124*(2), 1626–1652. https://doi.org/10.1029/2018jb016593

Tesauro, M., Audet, P., Kaban, M. K., Burgmann, R., & Cloetingh, S. (2012). The effective elastic thickness of the continental lithosphere: Comparison between rheological and inverse approaches. *Geochemistry, Geophysics, Geosystems*, *13*(9), Q0AN03. https://doi.org/10.1029/2012gc004162

Wang, Y., Liu, L., & Zhou, Q. (2022). Topography and gravity reveal denser cratonic lithospheric mantle than previously thought. *Geophysical Research Letters*, *49*(1), e2021GL096844. https://doi.org/10.1029/2021gl096844

Watkins, C. E., & Conrad, C. P. (2018). Constraints on dynamic topography from asymmetric subsidence of the mid-ocean ridges. *Earth and Planetary Science Letters*, *484*, 264–275. https://doi.org/10.1016/j.epsl.2017.12.028

Watts, A. B., & Burov, E. B. (2003). Lithospheric strength and its relationship to the elastic and seismogenic layer thickness. *Earth and Planetary Science Letters*, *213*(1–2), 113–131. https://doi.org/10.1016/s0012-821x(03)00289-9

West, B. P., Sempéré, J.-C., Pyle, D. G., Morgan, J. P., & Christie, D. M. (1994). Evidence for variable upper mantle temperature and crustal thickness in and near the Australian-Antarctic Discordance. *Earth and Planetary Science Letters*, *128*(3–4), 135–153. https://doi.org/10.1016/0012-821x(94)90141-4

White, R. S., McKenzie, D., & O'Nions, R. K. (1992). Oceanic crustal thickness from seismic measurements and Rare Earth Element inversions. *Journal of Geophysical Research*, *97*(B13), 19683–19715. https://doi.org/10.1029/92jb01749

Wildman, M., Brown, R., Beucher, R., Persano, C., Stuart, F., Gallagher, K., et al. (2016). The chronology and tectonic style of landscape evolution along the elevated Atlantic continental margin of South Africa resolved by joint apatite fission track and (U-Th-Sm)/He thermochronology. *Tectonics*, *35*(3), 511–545. https://doi.org/10.1002/2015tc004042

Wilson, J. W. P., Roberts, G. G., Hoggard, M. J., & White, N. J. (2014). Cenozoic epeirogeny of the Arabian Peninsula from drainage modeling. *Geochemistry, Geophysics, Geosystems*, *15*(10), 3723–3761. https://doi.org/10.1002/2014gc005283

Winterbourne, J. R., Crosby, A. G., & White, N. J. (2009). Depth, age and dynamic topography of oceanic lithosphere beneath heavily sedimented Atlantic margins. *Earth and Planetary Science Letters*, *287*(1–2), 137–151. https://doi.org/10.1016/j.epsl.2009.08.019

Winterbourne, J. R., White, N., & Crosby, A. (2014). Accurate measurements of residual topography from the oceanic realm. *Tectonics*, *33*(6), 982–1015. https://doi.org/10.1002/2013tc003372

Wyllie, M. R. J., Gregory, A. R., & Gardner, L. W. (1956). Elastic wave velocities in heterogeneous and porous media. *Geophysics*, *21*(1), 41–70. https://doi.org/10.1190/1.1438217

Yamauchi, H., & Takei, Y. (2016). Polycrystal anelasticity at near-solidus temperatures. *Journal of Geophysical Research: Solid Earth*, *121*(11), 7790–7820. https://doi.org/10.1002/2016jb013316

Yang, T., & Gurnis, M. (2016). Dynamic topography, gravity and the role of lateral viscosity variations from inversion of global mantle flow. *Geophysical Journal International*, *207*(2), 1186–1202. https://doi.org/10.1093/gji/ggw335

Zhu, L., & Kanamori, H. (2000). Moho depth variation in southern California from teleseismic receiver functions. *Journal of Geophysical Research*, *105*(B2), 2969–2980. https://doi.org/10.1029/1999jb900322

Zhu, R.-X., Yang, J.-H., & Wu, F.-Y. (2012). Timing of destruction of the North China craton. *Lithos*, *149*, 51–60. https://doi.org/10.1016/j.lithos.2012.05.013

Ziegler, P. A. (1992). European Cenozoic rift system. *Tectonophysics*, *208*, 91–111. https://doi.org/10.1016/b978-0-444-89912-5.50009-0